NASA TECHNICAL MEMORANDUM

NASA TM X-2671

NASA TM X-2671

HIGH-ALTITUDE FLIGHT TEST OF A DISK-GAP-BAND PARACHUTE DEPLOYED BEHIND A BLUFF BODY AT A MACH NUMBER OF 2.69

by Clinton V. Eckstrom and Darrell R. Branscome

Langley Research Center
Hampton, Va. 23365

NATIONAL AERONAUTICS AND SPACE ADMINISTRATION • WASHINGTON, D. C. • DECEMBER 1972

1. Report No.	2. Government Accession No.	3. Recipient's Catalog No.
NASA TM X-2671		

4. Title and Subtitle	5. Report Date
HIGH-ALTITUDE FLIGHT TEST OF A DISK-GAP-BAND PARACHUTE DEPLOYED BEHIND A BLUFF BODY AT A MACH NUMBER OF 2.69	December 1972
	6. Performing Organization Code

7. Author(s)	8. Performing Organization Report No.
Clinton V. Eckstrom and Darrell R. Branscome	L-8555
	10. Work Unit No. 709-16-02-02
9. Performing Organization Name and Address	11. Contract or Grant No.
NASA Langley Research Center Hampton, Va. 23365	
	13. Type of Report and Period Covered
12. Sponsoring Agency Name and Address	Technical Memorandum
National Aeronautics and Space Administration Washington, D.C. 20546	14. Sponsoring Agency Code

15. Supplementary Notes

With appendix B by Percy J. Bobbitt

16. Abstract

A flight test was conducted with a 16.8-meter-nominal-diameter (55-foot) disk-gap-band parachute located at a trailing distance of 4.4 forebody diameters behind a 4.57-meter-diameter (15-foot) bluff-body planetary entry aeroshell and attached instrumented payload. At the time of parachute deployment the aeroshell-payload combination was oscillating through an angle-of-attack range of $\pm 40^{\circ}$. Continued oscillatory motion of the aeroshell-payload combination and similar motion of the parachute caused rapid changes in parachute shape and loading which resulted in extensive cloth damage in the band and outer disk-edge areas of the parachute canopy. During steady-state descent the damaged parachute provided an effective-drag coefficient of about 0.33 which was about 60 percent of that expected. An appendix by Percy J. Bobbitt presents a theoretical analysis of the aerodynamic heating to be expected at the flow stagnation line of a disk-gap-band parachute at supersonic speeds.

17. Key Words (Suggested by Author(s))	18. Distribution Statement
Disk-gap-band parachute Parachute flight test Decelerator	Unclassified – Unlimited

19. Security Classif. (of this report)	20. Security Classif. (of this page)	21. No. of Pages	22. Price*
Unclassified	Unclassified	69	$3.00

*For sale by the National Technical Information Service, Springfield, Virginia 22151

HIGH-ALTITUDE FLIGHT TEST OF A DISK-GAP-BAND PARACHUTE DEPLOYED BEHIND A BLUFF BODY AT A MACH NUMBER OF 2.69

By Clinton V. Eckstrom and Darrell R. Branscome
Langley Research Center

SUMMARY

A flight test was conducted with a 16.8-meter-nominal-diameter (55-foot) disk-gap-band parachute located at a trailing distance of 4.4 forebody diameters behind a 4.57-meter-diameter (15-foot) bluff-body planetary entry type of aeroshell and attached instrumented payload. At the time of parachute deployment the aeroshell-payload combination was oscillating through an angle-of-attack range of $\pm 40^{\circ}$. The test parachute, which was mortar deployed, attained inflation and peak loading at a Mach number of 2.62 and a dynamic pressure of 929 N/m^2 (19.4 lbf/ft^2). Continued oscillatory motion of the aeroshell-payload combination and similar motion of the parachute caused rapid changes in parachute shape and loading which resulted in extensive cloth damage in the band and outer disk-edge areas of the parachute canopy. The cloth damage, most of which occurred during the first 4 seconds of the flight test, resulted in a significant reduction in parachute projected area and drag efficiency. The bluff-body aeroshell was released from the instrumented payload 7 seconds after parachute deployment. During steady-state descent with the instrumented payload the damaged parachute exhibited an average effective-drag coefficient of 0.33 which was about 60 percent of that expected. Postflight analysis led to the conclusion that the major cause of damage in the parachute disk-edge area was failure of the stitching joining the radial tapes to the disk edge with subsequent tearing of the gore cloth. In the band areas it is believed that the major cause of damage was the transfer of loads between adjacent gore structural tapes through the cloth panels in a diagonal direction. Aerodynamic heating causing reduced cloth strength is believed to have been a contributing factor. The theoretical analysis used to estimate aerodynamic heating at the flow stagnation line of the disk-gap-band parachute is included as an appendix by Percy J. Bobbitt.

INTRODUCTION

In the past few years the National Aeronautics and Space Administration has conducted several flight test programs to provide data on the performance of decelerator

systems in low-density environments at Mach numbers and free-stream dynamic pressures similar to those expected for a system operating in the atmosphere of the planet Mars. (See refs. 1 to 4.) These programs utilized both rocket-launched slender-body payloads and balloon-launched bluff-body aeroshell—slender-body payload combinations where the aeroshell was released from the payload at the time of parachute opening. These previous systems operated on an ascending flight path during the decelerator test period.

The purposes of the subject flight test were: (1) to determine the operating characteristics of a disk-gap-band parachute in the wake of a large bluff-body aeroshell and attached payload in a flight environment typical of a spacecraft entering the atmosphere of the planet Mars; and (2) to verify by flight test, on an entry flight path, a technique to provide a rocket-launched, erectable, bluff-body aeroshell—payload combination for use in qualification testing of full-scale decelerator systems to be used for a specific Mars mission.

This paper presents the physical and operational characteristics of the parachute system tested and an analysis of probable causes of the parachute damage which occurred. An evaluation of parachute damage is given in appendix A. Appendix B by Percy J. Bobbitt presents the theoretical analysis used prior to the flight test to evaluate the aerodynamic heating and parachute cloth temperature to be expected at the flow stagnation line of the disk-gap-band test parachute at the planned supersonic test velocities. Details about the rocket-launch vehicle and the erectable bluff-body aeroshell and their performance are presented in reference 5.

SYMBOLS

Values are given in both SI and U.S. Customary Units. The measurements and calculations were made in the U.S. Customary Units.

$C_{A,o}$ nominal axial-force coefficient

$C_{D,o}$ drag coefficient, average of calculated values of $C_{A,o}$

$(C_{D,o})_{eff}$ effective-drag coefficient (based on vertical descent velocity and acceleration)

D_1 forebody (aeroshell) diameter, m (ft)

D_2 estimated projected diameter of parachute at full inflation, m (ft)

D_o	nominal diameter of parachute, $(4S_o/\pi)^{1/2}$, m (ft)
E	aeroshell drag force, N (lbf)
F	forces measured by tensiometers, N (lbf)
g	acceleration due to gravity, 9.81 m/sec^2 (32.2 ft/sec^2)
l	decelerator trailing distance, m (ft)
m	mass, kg (slugs)
q_∞	free-stream dynamic pressure, $\frac{1}{2}\rho V_\infty^2$, N/m^2 (lbf/ft^2)
S_o	nominal surface area of parachute canopy including gap and vent, m^2 (ft^2)
S_p	projected area of parachute canopy, m^2 (ft^2)
t	time from vehicle lift-off, sec
t'	time from mortar firing, sec
V_∞	true airspeed, m/sec (ft/sec)
Z	local vertical axis, positive down
ρ	atmospheric density, kg/m^3 (slugs/ft^3)

Subscripts:

pl	payload
std	standard
t	total

Dots over symbols denote differentiation with respect to time.

TEST SYSTEM

The launch vehicle consisted of a Castor XM-33E2 rocket motor with two Recruit TE-M-29-1 assist rocket motors, an instrumented payload with an attached erectable forebody (aeroshell) and a jettisonable nose cone as shown in figures 1 and 2. A photograph of the rocket vehicle in the launch position is presented as figure 3. The weights of the various flight configurations are presented in table I, and the various flight conditions of time, velocity, Mach number, and altitude are presented in table II. The flight test sequence and the recorded times of significant events are presented in figure 4.

The umbrellalike erectable aeroshell was maintained in the folded position until the reentry portion of the flight test, as shown in figure 4. In the erected position the aeroshell formed a 120^{o} total angle blunted cone with a maximum diameter of 4.57 m (15 ft). An attitude control system (ACS) was utilized to reorient the vehicle attitude in a downward direction at flight apogee (as shown in fig. 4) and to hold this position so that it would be pointed in the direction of the flight path at the time of erection of the aeroshell forebody. After erection of the aeroshell and jettisoning of the nose cone the attitude control jets were no longer operational. It was planned that the spacecraft would then be maintained in the proper flight attitude by aerodynamic forces acting on the aeroshell forebody.

A redundant command receiver system in the instrumented payload section was utilized to perform three of the system functions shown in figure 4. These system functions commanded from the ground control center were:

(1) The erection of the aeroshell forebody

(2) Firing of the mortar system for deployment of the test parachute

(3) Activation of the payload ballast release mechanism to reduce system weight and facilitate recovery

The test parachute was stored in and deployed by a mortar system located at the aft end of the payload. The mortar volume available for storage of the packed parachute was 0.088 m^3 (3.12 ft^3). The expected in-flight pack ejection velocity, based on several preflight ground deployment tests, was about 46.9 m/sec (154 ft/sec) for a 57-kg (127-lbm) parachute pack and sabot assembly.

A complete description of the launch vehicle, the erectable aeroshell, the attitude control system, and other vehicle-associated hardware and an evaluation of their performance may be found in reference 5.

PAYLOAD INSTRUMENTATION

The payload instrumentation utilized to acquire data for the evaluation of the test parachute performance included the three tensiometers located on the aft bulkhead of the payload for direct measurement of loads in the parachute attachment risers, accelerometers along the three mutually perpendicular body axes, an attitude reference system, and four cameras. Data from the accelerometers, the tensiometers, and the attitude reference system were telemetered to ground recording stations, whereas the camera film was obtained after recovery of the payload from the impact area.

The three tensiometers located on the aft bulkhead were of the electrical strain-gage type with each calibrated from 0 to 71 200 N (0 to 16 000 lbf). The tensiometers (see fig. 5), were attached to the payload by means of a universal joint arrangement which allowed them to assume alinement with the parachute attachment riser during the parachute test period. Prior to parachute deployment the tensiometers were rotated and folded over on the payload bulkload and secured as shown in figure 6.

Payload accelerations were measured by servo-type accelerometers. Two accelerometers were alined with the longitudinal axis of the payload. The first, referred to as the high-range longitudinal accelerometer, was ranged to ±30 g-units. The other longitudinal accelerometer referred to as the low-range unit, was ranged to ±5 g-units. This lower range longitudinal accelerometer was included to provide more accurate data during portions of the test when accelerations were low. Two other accelerometers were mounted normal to the payload longitudinal axis and normal to each other and are referred to herein as the transverse accelerometer and the normal accelerometer, respectively. These normal and transverse accelerometers were also ranged to ±5 g-units.

The attitude reference system, referred to herein as the gyro platform, consisted of two two-degree-of-freedom gyros mounted on a common gimbal. During flight the gyro platform measured the attitude of the payload relative to an inertial reference.

Of the four payload cameras, two were pointed aft to record the parachute deployment process, the canopy inflation, and the subsequent parachute performance. Both of these aft-viewing cameras were started at the same time (1 sec prior to mortar firing); although one camera operated at 64 pictures per second (pps); and the other, at 16 pps. The faster frame rate camera was used primarily to acquire details of the high-frequency motion of the parachute during deployment and operation at supersonic velocities, whereas the slower frame rate camera (having the same length of film) was able to record events for a much longer period of time (100 sec versus 25 sec). A side-viewing payload camera (16 pps) was used to record the aeroshell erection.

The fourth camera (16 pps) was located in the nose of the payload to view the aeroshell as it separated from the payload.

Coded timing marks appeared on all the payload camera films and on the telemetry records recorded at the ground stations, thereby allowing correlation of events recorded on film with actual flight test times.

TEST PARACHUTE

Geometric Description

The test parachute was a disk-gap-band (DGB) design having a nominal diameter D_o of 16.8 m (55 ft) and a nominal canopy surface area S_o of 220.7 m^2 (2376 ft^2). The disk or center part of the canopy, which included the vent area, had a surface area equal to 53 percent of the nominal surface area S_o. The disk was a regular polygon with 42 sides (nearly a circle). The band part of the canopy, with a surface area equal to 35 percent of the nominal surface area S_o, was a right circular cylinder with a circumference equal in length to the perimeter of the disk part of the canopy. The disk and the band were separated by a gap or open area equal to 12 percent of the nominal surface area S_o. There was also a vent at the center of the disk with an open area equal to 0.5 percent of the nominal surface area S_o. The total open area or geometric porosity of the canopy was therefore 12.5 percent of the nominal surface area S_o.

Figure 7 presents the general parachute and aeroshell-payload configuration. General characteristics of the test parachute are presented in table III. Figure 8 (see table IV) presents the dimensional details of a gore.

Construction Materials and Weights

The test parachute was fabricated of type 52 high-tenacity Dacron materials except for the center section of the disk which was fabricated of Nomex cloth. Characteristics of the component materials are presented in table IV. The weight breakdown of the parachute system is presented in table V.

RESULTS AND DISCUSSION

Test Data

The flight test vehicle was launched at 1:57 p.m. e.s.t., on October 9, 1970, from the NASA Wallops Station, Virginia, test site. Histories of payload altitude and relative velocity for the first 400 seconds of the flight, as measured by FPS-16 radar, are shown in figure 9. Figure 4 presented the flight sequence and the recorded times for the significant flight events.

Meteorological data used in analysis of the parachute performance were attained by means of an Arcasonde sounding rocket payload launched at 2 hours and 55 minutes after

the parachute flight test launch time. These data were supplemented by data from a radiosonde which was released 3 hours and 34 minutes before the flight test vehicle was launched. The atmospheric density as derived from the measured temperature profiles is shown in figure 10 as a ratio to the 1962 U.S. Standard Atmosphere values (ref. 6). The wind profile as determined from both the Arcasonde and radiosonde soundings is presented in east-west and north-south components in figure 11.

The estimated uncertainty of the derived density ranges from ±3 percent at ground level to about ±6 percent at 54 km (177 165 ft). The estimated uncertainty of the measured wind values are ±5 percent from ground level to about 30-km (98 425-ft) altitude and increase to about ±10 percent over the range from 30-km (98 425-ft) to 50-km (164 040-ft) altitude.

The measured atmospheric data were used with the radar track data to determine histories of payload true airspeed (fig. 12), Mach number (fig. 13), and dynamic pressure (fig. 14) during the 20-second period immediately after initiation of parachute deployment. By definition, the initiation of parachute deployment corresponds to mortar firing ($t' = 0$). Parachute deployment was initiated at a true airspeed of 884 m/sec (2900 ft/sec), a Mach number of 2.69, a dynamic pressure of 876 N/m^2 (18.3 lbf/ft^2), and an altitude of 44.29 km (145 300 ft) above mean sea level. The first peak load associated with full opening of the parachute canopy came at $t' = 1.22$ seconds at which time the test conditions were a true airspeed of 855 m/sec (2805 ft/sec), a Mach number of 2.62, a dynamic pressure of 929 N/m^2 (19.4 lbf/ft^2), and an altitude of 43.35 km (142 235 ft) above mean sea level. The estimated uncertainty of these test conditions is about ±1 percent for the Mach number and ±5 percent for the dynamic pressure, based on a ±1-percent velocity error, a ±2-percent temperature error, a ±4-percent density error, and by using a first-order error analysis.

The history of forces transmitted to each of the three riser line tensiometers and the direct summation of these forces for the first 20 seconds after initiation of parachute deployment are presented in figure 15. The first small peak deployment load at $t' = 0.12$ second is believed to be associated with the full-length deployment of the risers and tensiometers from their storage location on the aft deck of the payload. The second small peak deployment load (snatch force) of 9070 N (2040 lbf) at $t' = 0.51$ second is associated with full-length deployment of the suspension lines (line stretch) and the beginning of canopy deployment. The loads associated with the parachute opening process begin at about $t' = 0.86$ second with the first peak opening load of 95 640 N (21 500 lbf) occurring at $t' = 1.22$ seconds. This first peak load is associated with the first opening of the parachute canopy. Three more peak loads were encountered immediately thereafter. These loads (fig. 15) were associated with the varying parachute frontal area, the continued increase in free-stream dynamic pressure, and the elasticity of the system

(particularly the parachute suspension lines). The last of these first four peak loads associated with the opening process was the largest loading encountered. This largest peak load was 103 770 N (23 330 lbf) at $t' = 1.42$ seconds. Thereafter the riser loads were of less magnitude, partly because the damage sustained by the parachute resulted in reduced frontal area and later because of the reduced free-stream dynamic pressure.

The histories of accelerations recorded by the accelerometers in the payload are presented in figure 16. The magnitudes of the accelerations shown are due in part to the deceleration forces imparted by the parachute to the aeroshell-payload combination and partly from the rapidly changing aeroshell-payload angular position (high angular rates). The large peak in longitudinal deceleration at $t' = 6.91$ seconds is associated with the release of the payload from the aeroshell, which resulted in a 44-percent reduction in system mass (1194 kg to 668 kg (2631 lbm to 1472 lbm)).

The payload angular positions with respect to the flight path were determined by the procedure given in reference 7 and are presented in figure 17.

Analysis of Parachute Performance

The disk-gap-band parachute was flight tested behind the bluff-body aeroshell and attached payload for a period of 7 seconds after which the bluff-body aeroshell was released. During the flight test the parachute was damaged at the outer disk edge and in the band area. About half of the gores were damaged at the disk-edge area and all of the gores in the band area were damaged. Some damage occurred during the first opening of the parachute but most of the damage occurred in a progressive manner in the interval immediately after the first opening. By the end of the first 4 seconds of the flight test most of the damaged areas of the parachute could be identified on the aft-camera film. An analysis of the various aspects of the parachute performance are presented in this section and an analysis of the parachute damage in the following section.

Parachute deployment.- Based on a total suspension line plus attachment system length of 19.7 m (64.6 ft) and a measured time to line stretch of 0.51 second, the average deployment velocity from mortar firing to line stretch was 39 m/sec (126 ft/sec). The resulting snatch force was 9070 N (2040 lbf).

Parachute inflation.- Selected frames from the aft-camera film showing the initial stages of parachute deployment, inflation, shape distortions, and damage propagation sequences are presented in figure 18.

The parachute projected-area-ratio history as determined from the aft-camera film is presented in detail in figure 19 for the inflation sequence and for a short interval thereafter. A more general presentation of the parachute projected-area-ratio history for the total 20 seconds after mortar firing is presented in figure 20. The solid lines between

data points in figures 19 and 20 represent intervals where the parachute canopy was in the camera field of view from frame to frame. The blank spaces between data points represent intervals where the parachute canopy is partly or totally out of view of the payload camera. A dashed line was used in the interval of the initial parachute opening from $t' = 0.95$ to 1.19 seconds during which the parachute is not in the field of view of the payload camera to indicate that the projected-area-ratio curve probably continues to grow smoothly. This is believed to be so even though the tensiometer forces have a peak at 1.09 seconds, a minimum at 1.17 seconds, and the first large peak at 1.22 seconds. Similar variations in transmitted parachute loads occurred during the parachute opening process of the flight tests of references 3, 4, and 8 even though the parachute projected-area-ratio growth continued smoothly during this interval. The variations in tensiometer forces during this interval are believed to be due primarily to the elasticity of the parachute suspension lines.

As can be seen from figure 18(c) at $t' = 1.21$ seconds, the parachute did not reach a complete inflation at all places around the outer edges of the canopy. Because of parachute damage that began at the first opening and progressed rapidly thereafter, the first opening was the maximum attained for the entire flight. Therefore an estimate was made of what the final projected area should have been by circumscribing a circle around the nearly fully opened parachute canopy as shown in figure 18(c) at $t' = 1.21$ seconds. The values of projected-area ratio shown in figures 19 and 20 are based on the estimated full-open parachute projected area.

Drag efficiency.- The axial-force coefficient $C_{A,o}$ of the parachute is presented in figure 21 for the first 20 seconds after mortar firing. The values of $C_{A,o}$ were determined for a nonelastic two-body system by using the equation

$$C_{A,o} = \frac{\Sigma F\left(m_t/m_{pl}\right)}{q_\infty S_o} + \frac{\left[\left(m_t/m_{pl}\right) - 1\right]E}{q_\infty S_o}$$

The second term of the right-hand side of the equation was applicable only for the first 7 seconds of the parachute flight test where the bluff aeroshell remained attached to the payload. After release of the aeroshell, the drag of the slender-body instrumented payload was neglected and only the first term of the right-hand side of the equation was applicable. (Data on the performance of the erected aeroshell-payload combination prior to parachute deployment are presented in ref. 5.)

Average values of the parachute axial-force coefficient $C_{A,o}$ were determined at a Mach number interval of 0.05 over the 20-second data period, and these average values are presented in figure 22 for the drag coefficient $C_{D,o}$ as a function of Mach number.

Previously established wind-tunnel data from reference 9 are provided in figure 22 for comparison purposes.

The vertical-descent velocity and the parachute effective-drag coefficient $(C_{D,o})_{eff}$ during steady-state descent are presented in figure 23. The values of effective-drag coefficient were determined by using the equation

$$(C_{D,o})_{eff} = \frac{2m_t}{\rho(\dot{Z})^2 S_o}(g - \ddot{Z})$$

As shown in figure 23, the test parachute provided an average effective-drag coefficient of 0.33, a value which represents about 60 percent of that expected for an undamaged parachute of the disk-gap-band configuration tested (ref. 10). The scatter in the data for $(C_{D,o})_{eff}$ increased at the lower altitudes because small variations or errors in measured descent velocities result in large changes in the values of $(C_{D,o})_{eff}$ as determined by the preceding equation.

Stability.- At the time of parachute deployment the aeroshell-payload combination was oscillating through an angle-of-attack range of $\pm 40^o$. The oscillatory motion of the aeroshell-payload combination continued after deployment of the test parachute with the parachute soon exhibiting somewhat similar motion. The angular motion of the deployed parachute was obtained by first using the payload aft-camera film to determine the attitude of the parachute with respect to the forebody and then, by time correlation with the aeroshell-payload attitude data (from the gyro platform), determining the parachute position with respect to the flight path. The parachute and the aeroshell-payload pitch- and yaw-attitude data are shown in figure 24 for the first 10 seconds after mortar firing.

The attitude data shown in figure 24 include a correction (plus 3.7^o yaw angle and minus 3.2^o pitch angle) based on a determination of the center of oscillation of the aeroshell-payload combination during the interval immediately prior to deployment of the test parachute. The pitch angle is in the vertical plane of the vehicle flight path and the yaw angle is in a plane perpendicular to the vertical plane. The aeroshell-payload combination was in a noseup and nose-left attitude (in this paper a negative value of pitch and positive value of yaw) with respect to the flight path at the instant of mortar firing. The parachute was therefore deployed below and to the right side of the flight path. During the interval from $t' = 0$ to about $t' = 0.75$ second, the unfurling parachute remained below and to the right of the flight path, essentially in the orientation in which it was deployed. As the parachute inflation sequence began (at about $t' = 0.83$ sec), the parachute became alined with the flight path; and after the first inflation of the parachute at $t' = 1.21$ seconds, the parachute motion closely followed the motion of the forebody. Dur-

ing the time interval immediately following the first inflation the parachute experienced its most extreme motions. It was also during this time interval (from $t' = 1.21$ sec to about $t' = 4.00$ sec) that the majority of the canopy damage occurred. Evaluation of the aft-camera film indicated that there were abrupt and severe changes in parachute canopy shape associated with the rapidly changing attitude of the parachute and forebody, and, in at least one instance, damage did occur to a particular area of the canopy as the shape change took place (fig. 18(c), frames 77 to 79).

Parachute Damage Analysis

Damage description.- Damage to the test parachute canopy occurred along the outer edge of the disk and to all areas of the band. The center or Nomex portion of the disk was undamaged. There were no tensile failures of any of the primary load-carrying structural members of the parachute (suspension lines, radial tapes, and circumferential tapes). However there were several failures of the stitching joining the radial tapes to the parachute canopy. Stitching failures occurred at 27 of the 42 radial tapes at the outer edge of the disk and at nine of the radial tapes at the upper band edge. Figure 25, a photograph of two gores, shows typical damaged areas. Figure 26, a sketch of the parachute canopy, indicates all of the damaged areas. The times at which damage could first be identified in different parts of the parachute are listed in table VI.

Damage causes.- After the test parachute opened, it exhibited rapid changes in shape and frontal area (figs. 18 and 19) and position relative to the aeroshell-payload combination and the flight path (fig. 24). These changes in parachute shape, frontal area, and angular position resulted in a continually shifting pattern of parachute loading and the frequent transfer of loads between adjacent canopy gores through the gore tapes and the cloth panels. Also this changing pattern of parachute loading resulted in shear-type loads between the radial tapes and the circumferential hem tapes. The major cause of damage occurring at the disk-edge area was failure of the stitching joining the radial tapes to the adjacent gore cloth. In the band area it is believed that the major cause of damage was the transfer of loads between adjacent gores across the cloth panels in a diagonal direction. A discussion of initial failure points and damage propagation is presented in more detail in appendix A.

Aerodynamic heating.- Prior to the flight test an analysis was made of the aerodynamic heating environment to be expected for the test parachute. This analysis, presented as appendix B, indicated that temperatures would approach 205° C (400° F) in the central area of the disk part of the parachute canopy. On the basis of this analysis and experience gained on a previous flight test (ref. 3) Nomex cloth was used in the central disk area of the canopy (as shown in fig. 8), and there were also three circumferential reinforcement tapes located in this area to act as rip stops and to prevent propagation of

any cloth damage that might occur in this area. As was mentioned previously, no damage occurred in this reinforced section.

With the knowledge that the center section of the canopy would encounter significant aerodynamic heating, it was expected that the other areas of the parachute would also be subjected to some elevated temperatures, although no problems in other areas were encountered on the previous flight test (ref. 3). For this flight test there was considerable evidence of localized material melting or burning on the damaged areas of the parachute cloth. Because of the localized nature of the burn areas it is believed that the burns noted resulted from friction burning (torn pieces of canopy cloth flailing in the airstream and against the remaining cloth panels, thereby causing surface burns in local areas) rather than from aerodynamic heating. However the Dacron cloth materials may have been considerably degraded in strength as a result of elevated temperatures caused by aerodynamic heating.

CONCLUSIONS

The disk-gap-band parachute having a nominal diameter of 16.8 meters (55 feet) was mortar deployed and flight tested behind a 4.57-meter-diameter (15-foot) bluff-body aeroshell and attached payload at a trailing distance of 4.4 forebody diameters for a period of 7 seconds after which the bluff-body aeroshell was released. Some specific conclusions are:

1. At the time of parachute deployment the aeroshell-payload combination was oscillating through an angle-of-attack range of $\pm 40^{o}$.

2. The test parachute attained opening and encountered first peak loading at 1.22 seconds, at which time the free-stream conditions were a Mach number of 2.62 and a dynamic pressure of 929 N/m^2 (19.4 lbf/ft^2).

3. Continued oscillatory motion of the aeroshell-payload combination after parachute deployment and similar motion of the parachute caused rapid changes in parachute shape and projected area. These motions resulted in a continually shifting pattern of parachute loading and the frequent transfer of loads between adjacent canopy gores through the gore tapes and the canopy cloth.

4. The test parachute sustained some cloth damage around the outer edge of the disk area during the first opening process, and by the end of the first 4 seconds of the flight test considerable additional cloth damage had occurred to the test parachute at both the outer disk-edge area (about half of the gores) and to the band area (all of the gores).

5. Because of the parachute damage which occurred, the parachute frontal area attained during the first opening was the maximum attained for the entire flight test.

6. The major cause of damage occurring at the disk-edge area was failure of the stitching joining the radial tapes to the disk edge with subsequent tearing of the gore cloth.

7. The major cause of damage which occurred in the band area of the parachute is believed to have been the transfer of loads between adjacent gores across cloth panels in a diagonal direction.

8. Aerodynamic heating is believed to have been a contributing cause to the parachute damage because of degraded cloth strength resulting from elevated temperatures.

9. Despite the extensive parachute damage which occurred, the average effective-drag coefficient was about 0.33, a value which represents about 60 percent of that expected for an undamaged parachute of the disk-gap-band configuration tested.

Langley Research Center,
National Aeronautics and Space Administration,
Hampton, Va., December 6, 1972.

APPENDIX A

PARACHUTE DAMAGE EVALUATION

Examination of the damaged parachute indicated that at the disk edge there were radial tape to circumferential hem tape stitching failures at 27 of the 42 gores. These stitching failures between the radial tapes and the disk edge are believed to have been the initial failure point for most of the damage incurred in the disk-edge area. An evaluation was made of the cloth tear propagation and the effectiveness of the diagonal gore panel seams in stopping the tears.

The seams joining the various cloth panels in each gore were at an angle of 45^{o} to the gore center line because the parachute was constructed with the cloth on the bias. To provide symmetry the panel seams were placed in opposite directions on every other gore as shown in figure 27. As a result of the opposite placement of gore panels there was a difference in the relationship of the panel seams to the radial tape at the corner of each gore at the outer disk edge. The two different corner configurations are labeled X and Y in figure 27.

There were 15 places where the radial tape stitching failures were at an X-corner configuration. At 12 of these 15 places the cloth tears propagated on both sides of the radial tape (24 tears). At two places the tears were small on one side of the tape but did propagate on the opposite sides (two tears). In one place the stitching failure extended a distance of less than 2 cm (0.75 in.), and no tears were initiated in the adjacent cloth panels. In one instance a cloth panel adjacent to an X-corner was damaged extensively even though the radial tape stitching remained intact. This was the D cloth panel in gore 32. It may be noted from table VI that the failure in gore 32 was the last to occur in the disk-edge area.

Cloth tears did propagate at a total of 27 places in the D cloth panels. At 21 of these places the tears were stopped by the diagonal seams between the D and E cloth panels. At five places the tears did propagate into the E cloth panel but the tears were stopped by the circumferential reinforcement tape and panel seam between cloth panels E and F. Note that the cloth panels C, D, and E were of Dacron material, whereas the panels above the reinforcement tape were of Nomex cloth.

There were 12 places where the radial tape stitching failures were at a Y-corner configuration. At nine of these places the resultant cloth tears did not propagate past the adjacent diagonal seams between the C and D cloth panels. At the other three places the cloth tears did propagate past the panel seam on one side but not on the other. The diagonal seams between cloth panels C and D were effective rip stops in 21 of the 24 places where cloth tears occurred in the C cloth panel.

In the band area of the canopy it was not possible to identify the initial points of failure as was done in the canopy disk-edge area. It appeared from the aft-camera film that the cloth failures started by separation of the upper band edge hem tape from the cloth in the B panel. However the band area of the parachute was not generally sufficiently visible to determine conclusively the sequence of failure. The diagonal seams between the cloth panels A and B remained intact in all but four places even though all of the band area cloth panels A and B were damaged with the exception of the A cloth panel of gore 38. In most gores the B cloth panel was the most severly damaged. There were nine places at which the radial tape stitching failed at the upper edge of the band. These stitching failures occurred at radial tapes 6 to 9 and tapes 12 to 16. Note that the band panels were fabricated of the lighter weight Dacron cloth.

APPENDIX B

THEORETICAL ANALYSIS OF THE AERODYNAMIC HEATING AT THE FLOW STAGNATION LINE OF A DISK-GAP-BAND PARACHUTE AT SUPERSONIC SPEEDS

By Percy J. Bobbitt
Langley Research Center

INTRODUCTION

A simple method of determining the equilibrium surface temperature at the stagnation line of a disk-gap-band parachute is presented. The analysis provides a better understanding of the fabric failure which occurred during the flight test of the disk-gap-band parachute discussed in the main body of this paper and an earlier one reported in reference 3.

It was concluded following the test described in reference 3 that aerodynamic heating had degraded the strength of the fabric of the test parachute. Rips which occurred from 2 to 4 seconds after the initiation of deployment and fabric stiffness (or hardening) located in the region of flow stagnation in the disk area of the test canopy supported this conclusion. Since no known method was available to evaluate this phenomenon and additional high Mach number tests were being planned, including the present one, the simplified stagnation-line heating analysis described in this appendix was undertaken.

SYMBOLS

a	speed of sound, m/sec (ft/sec)
c	velocity gradient, a_δ/x_o, 1/sec
c_p	specific heat of air at constant pressure, joules/kg-K (Btu/slug-^oR or ft^2/sec^2-^oR)
D_o	nominal diameter of parachute, m (ft)
h	enthalpy, m^2/sec^2 (ft^2/sec^2)
$I(1) = (N_{Pr})^{-1/3}$	

$$J(1) = \frac{(N_{Pr})^{-1/2}}{2}$$

k	thermal conductivity of air, joules/m-sec-K (Btu/ft-sec-^{o}R)
M	Mach number, V/a
N_{Pr}	Prandtl number, $\mu c_p/k$
q_c	convective-heating rate, joules/m^2-sec (Btu/ft^2-sec)
q_r	radiative-heating rate, joules/m^2-sec (Btu/ft^2-sec)
T	temperature, K (^{o}R)
u,v	velocity components parallel and normal to surface, respectively, in vicinity of stagnation point, m/sec (ft/sec)
V	velocity, m/sec (ft/sec)
x,y	distances along or normal to surface, respectively, measured normal to stagnation line, m (ft)
x_o	distance from stagnation line to edge of vent, m (ft)
δ	distance of shock from stagnation point, m (ft)
ϵ	surface emissivity
μ	dynamic viscosity, kg/m-sec (lbm/ft-sec)
ν	kinematic viscosity, μ/ρ, m^2/sec (ft^2/sec)
ρ	density, kg/m^3 (slugs/ft^3)
σ	Stephan-Boltzmann radiation constant, joules/m^2-sec-K^4 (Btu/ft^2-sec-^{o}R^4)
ϕ''	function of y which has value of 1.23 at $y = 0$ (see eq. (5))

Subscripts:

e	value at edge of boundary layer in vicinity of stagnation line
o	value at stagnation line
s	values at edge of boundary layer at stagnation line
sl	sea-level value
w	value at surface
δ	value immediately downstream of shock
∞	free-stream value

ANALYSIS

The basic equation necessary to obtain the stagnation-line convective heating rate is the Fourier law for conduction at the wall

$$q_c = k_w\left(\frac{\partial T}{\partial y}\right)_w \tag{1}$$

Equation (1) may be written in a more useful form by using the relation $h = c_p T$ and the definition of Prandtl number

$$q_c = \frac{\mu_w}{N_{Pr,w}}\left(\frac{dh}{du}\right)_w\left(\frac{\partial u}{\partial y}\right)_w \tag{2}$$

In subsequent equations, subscripts on N_{Pr} are not used because it varies negligibly over the temperature range of concern herein. A solution to the viscous-flow equations may now be employed to relate the velocity derivative of the wall enthalpy to the velocity and enthalpy at the wall and extremity of the boundary layer. Van Driest (ref. 11) obtained the following solution by using the Crocco method

$$\left(\frac{dh}{du}\right)_w = \frac{1}{u_e I(1)}\left[h_e + N_{Pr}J(1)u_e^2 - h_w\right] \tag{3}$$

If the flow in the region of the stagnation line is assumed to be two dimensional, as depicted in figure 28(a), an expression for $(\partial u/\partial y)_w$ is obtainable from the analysis given in reference 12 or 13 and is

$$\left(\frac{\partial u}{\partial y}\right)_w = \sqrt{\frac{c}{\nu}}\, u_e(\phi'')_{y=0} \tag{4}$$

The function ϕ'' is tabled in references 12 and 13 as a function of the stretched coordinate $\sqrt{\frac{c}{\nu}}\, y$. At the surface, that is, $y = 0$, the function ϕ'' has the value 1.23; therefore

$$\left(\frac{\partial u}{\partial y}\right)_w = 1.23 u_e \sqrt{\frac{c}{\nu}} \tag{5}$$

The constant c in equation (5) is equivalent to the normal and tangential velocity gradients since the velocities in the region of the stagnation point are given by

$$u = cx \tag{6}$$

$$v = cy \tag{7}$$

Two ways of estimating the velocity gradient are available: One is to require the velocity normal to the surface to be linear from the stagnation line to the shock; the other is to require $u = a_\delta$ at $x = x_o$ (see fig. 28). The latter condition was chosen since it is not likely that the velocity v will vary linearly from the stagnation line to the shock plus the fact that the vent at the top of the canopy will obviously have an overriding influence on the flow in the stagnation region. Consequently, c is determined by

$$c = \frac{a_\delta}{x_o} \tag{8}$$

and

$$\left(\frac{\partial u}{\partial y}\right)_w = 1.23 u_e \sqrt{\frac{a_\delta}{x_o \nu}} \tag{9}$$

In the analysis of reference 12, ν is taken to be constant; hence, in the present analysis, it is necessary to stipulate whether the ν in equation (9) should be evaluated at the wall or external to the boundary layer. The former alternative was chosen. If equations (9) and (3) are substituted into equation (2), the equation for q_c becomes

$$q_c = \frac{1.23\sqrt{\frac{a_\delta}{x_o}}\sqrt{\rho_w \mu_w}\left[h_e + N_{Pr}J(1)u_e^2 - h_w\right]}{N_{Pr}I(1)} \tag{10}$$

The stagnation-line heating rate may now be written by inspection of equation (10) as

$$q_{c,o} = \frac{1.23\sqrt{\frac{a_\delta}{x_o}}\sqrt{\left(\rho_w \mu_w\right)_o}}{N_{Pr}I(1)}\left(h_s - h_w\right) \tag{11}$$

Additional modifications to equation (11) required before the computational equation for $q_{c,o}$ is obtained are:

(1) The denominator of equation (11), often termed Reynolds' analogy factor, is approximated by $(N_{Pr})^{2/3}$ (see ref. 11)

(2) N_{Pr} is set equal to 0.7

(3) h_s and h_w are replaced by $\frac{V_\infty^2}{2} + c_{p,\infty}T_\infty$ and $c_{p,w}T_w$, respectively

With these changes and casting many of the quantities in nondimensional form, the final form of $q_{c,o}$ is given by

$$q_{c,o} = \frac{0.002\rho_\infty V_\infty \sqrt{\frac{\rho_s}{\rho_\infty}\frac{a_\delta}{a_\infty}\frac{\mu_s}{\mu_\infty}}\sqrt{\frac{\left(\rho_w \mu_w\right)_o}{\rho_s \mu_s}}\left(\frac{V_\infty^2}{2} + c_{p,\infty}T_\infty - c_{p,w}T_{w,o}\right)}{\sqrt{M_\infty \frac{x_o}{D_o}}\sqrt{\frac{\rho_\infty V_\infty D_o}{\mu_\infty}}} \tag{12}$$

when the numerical constant has been adjusted to yield $q_{c,o}$ in Btu/ft^2-sec. The nondimensional quantities and the free-stream viscosity are determined from the following equations:

$$\frac{\rho_s}{\rho_\infty} = \frac{6M_\infty^2}{M_\infty^2 + 5}\left[\frac{36M_\infty^2}{5\left(7M_\infty^2 - 1\right)}\right]^{5/2}$$

$$\frac{a_\delta}{a_\infty} = \frac{\left[\left(7M_\infty^2 - 1\right)\left(M_\infty^2 + 5\right)\right]^{1/2}}{6M_\infty}$$

$$\frac{\mu_s}{\mu_\infty} = \frac{T_\infty + 216}{\frac{M_\infty^2 + 5}{5} T_\infty + 216} \left(\frac{M_\infty^2 + 5}{5}\right)^{3/2}$$

$$\frac{(\rho_w \mu_w)_o}{\rho_s \mu_s} = \left(\frac{\frac{M_\infty^2 + 5}{5} T_\infty + 216}{T_{w,o} + 216}\right)\left(\frac{T_{w,o}}{T_\infty} \frac{5}{M_\infty^2 + 5}\right)^{1/2}$$

$$\mu_\infty = \mu_{sl}\left(\frac{T_{sl} + 216}{T_\infty + 216}\right)\left(\frac{T_\infty}{T_{sl}}\right)^{3/2}$$

These equations make use of the Sutherland viscosity law and a ratio of specific heats of 1.4.

Generally, to determine the temperature of the surface of a body being subjected to aerodynamic heating requires that the rate at which heat is being absorbed be equated to the difference between the rate at which heat is convected to the surface and the rate at which it is radiated away. The parachute which is fabricated of a very thin material has little heat-storage capacity; therefore, its surface temperature will, within a few seconds, approach the radiative-convective equilibrium value, that is, the temperature which satisfies the relation

$$q_r = q_c \tag{13}$$

With $q_r = \sigma \epsilon T_w^4$, the stagnation-line temperature $T_{w,o}$ is given by

$$T_{w,o} = \left(\frac{q_{c,o}}{\epsilon \sigma}\right)^{1/4} \tag{14}$$

The use of the preceding equations yields a result for $T_{w,o}$ which does not account for the heat radiated to a point on the stagnation line from other parts of the canopy nor the heat radiated from the back side of the parachute. As may be noted in equation (12), $q_{c,o}$ is a function of $T_{w,o}$ so that equations (14) and (12) must be solved iteratively.

Because the fabric does have some heat capacity, the equilibrium temperature values calculated are conservative for the first few seconds after the parachute is open and

operating. If the parachute is lightly loaded and decelerates rapidly, then deployment Mach numbers as high as that of the present test may be tolerated without damage. (See ref. 8.) If the calculated values of equilibrium temperature indicate a problem, then a transient analysis would be advisable. Transient temperature values may be obtained with the aid of equation (12) and by accounting for heat conduction and storage in the fabric.

CALCULATED RESULTS

Calculated results discussed herein are for a symmetrical, fully inflated, disk-gap-band parachute similar to that sketched in figure 7. Equilibrium stagnation-line temperatures were determined for the worst case heating and loads trajectory anticipated for the flight test reported in the main text of this paper. For the calculations presented, the material emissivity constant ϵ was assumed to be 0.8.

The location of the stagnation line was estimated with the aid of figure 29 which shows the area of stiffened material on the parachute deployed at $M = 3.31$ as reported in reference 3. It was assumed that the stagnation line was located midway between the inner and outer edges of the stiffened region; the average value of x_o was 0.88 m (2.9 ft). This was for a parachute having a nominal diameter of 12.2 m (40 ft), a disk diameter of 8.88 m (29.12 ft), and a vent diameter of 0.86 m (2.82 ft). The test parachute herein had a nominal diameter of 16.8 m (55 ft) and other dimensions as listed in table III and shown in figure 8. The distance of the stagnation line from the vent edge was scaled up accordingly.

Tabulations of the trajectory and atmospheric input data used in the calculations are given in table VII. A plot of the calculated equilibrium surface temperatures as a function of time is presented in figure 30.

As shown in figure 30, equilibrium temperatures at the flow stagnation line of greater than 204° C (400° F) were predicted. Because of the limited load-carrying capability of Dacron at higher temperatures, Nomex cloth (high-temperature resistant nylon) was used in the fabrication of the central section of the disk area of the test parachute as shown in figure 27. A comparison of the worst case trajectory presented in table VII and the actual trajectory flown indicates that the calculated equilibrium temperatures should not have been exceeded.

REFERENCES

1. Murrow, Harold N.; and McFall, John C., Jr.: Some Test Results From the NASA Planetary Entry Parachute Program. J. Spacecraft & Rockets, vol. 6, no. 5, May 1969, pp. 621-623.

2. Whitlock, Charles H.; and Bendura, Richard J.: Inflation and Performance of Three Parachute Configurations From Supersonic Flight Tests in a Low-Density Environment. NASA TN D-5296, 1969.

3. Eckstrom, Clinton V.: Flight Test of a 40-Foot-Nominal-Diameter Disk-Gap-Band Parachute Deployed at a Mach Number of 3.31 and a Dynamic Pressure of 10.6 Pounds Per Square Foot. NASA TM X-1924, 1970.

4. Eckstrom, Clinton V.: High-Altitude Flight Test of a 40-Foot-Diameter (12.2-Meter) Ringsail Parachute at a Deployment Mach Number of 2.95. NASA TN D-5796, 1970.

5. Henning, Allen B.; and Lundstrum, Reginald R. (With appendix A by James C. Young): Flight Test of an Erectable Spacecraft Used for Decelerator Testing at Simulated Mars Entry Conditions. NASA TN D-6910, 1972.

6. Anon.: U.S. Standard Atmosphere, 1962. NASA, U.S. Air Force, and U.S. Weather Bur., Dec. 1962.

7. Preisser, John S.: Determination of Angles of Attack and Sideslip From Radar Data and a Roll-Stabilized Platform. NASA TM X-2514, 1972.

8. Eckstrom, Clinton V.; and Preisser, John S.: Flight Test of a 40-Foot-Nominal-Diameter Disk-Gap-Band Parachute Deployed at a Mach Number of 2.72 and a Dynamic Pressure of 9.7 Pounds Per Square Foot. NASA TM X-1623, 1968.

9. Bobbitt, P. J.; Mayhue, R. J.; Faurote, G. L.; and Galigher, L. L.: Supersonic and Subsonic Wind-Tunnel Tests of Reefed and Unreefed Disk-Gap-Band Parachutes. AIAA Paper No. 70-1172, Sept. 1970.

10. Preisser, John S.; and Grow, R. Bruce: High-Altitude Flight Test of a Reefed 12.2-Meter-Diameter Disk-Gap-Band Parachute With Deployment at a Mach Number of 2.58. NASA TN D-6469, 1971.

11. Van Driest, E. R.: Investigation of Laminar Boundary Layer in Compressible Fluids Using the Crocco Method. NACA TN 2597, 1952.

12. Schlichting, H.: Lecture Series "Boundary Layer Theory." Part 1 – Laminar Flows. NACA TM 1217, 1949.

13. Hiemenz, K.: Die Grenzschicht an einem in der gleichförmigen Flüssigkeitsstrom eingetauchten geraden Kreeiszylinder. Dinglers Polytech. J., vol. 326, 1911, p. 322.

TABLE I.- CONFIGURATION MASSES

Configuration	Mass	
	kg	lbm
Total vehicle at launch	6688	14 745
Total vehicle after burnout of motors	3077	6 783
Spacecraft after motor and adapter section separation	1389	3 062
Spacecraft after aeroshell erection and nose cone separation	1196	2 637
Spacecraft and parachute system after parachute ejection and separation of the mortar sabot	1194	2 631
Payload and parachute system after aeroshell separation	668	1 472
Payload and parachute system after ballast separation	315	694

TABLE II.- FLIGHT TEST CONDITIONS

Item	Event	Flight time, sec	Velocity		Mach no.	Altitude	
			m/sec	ft/sec		km	ft
1	Launch	0	0	0	0	0	0
2	Maximum velocity	≈36	1175	3855	4.02	21.09	69 200
3	Vehicle separation	90.08	735	2410	2.37	65.82	215 930
4	Begin aeroshell erection	224.50	846	2775	2.56	56.31	184 730
5	Complete nose cone separation	225.18	852	2795	2.58	55.81	183 100
6	Parachute mortar firing	240.31	884	2900	2.69	44.29	145 300
7	First parachute opening	241.53	855	2805	2.62	43.35	142 235
8	Aeroshell separation	247.23	587	1925	1.84	39.68	130 180
9	Ballast separation	1099.41	14	47	.04	4.91	16 110
10	Surface impact	≈1655	----	----	----	0	0

TABLE III.- PARACHUTE CHARACTERISTICS

Parachute type	Disk-gap-band	
Number of gores and suspension lines	42	
Nominal diameter, D_o, m (ft)	16.8	(55)
Nominal area, S_o, m^2 (ft^2)	220.7	(2376)
Disk area (including vent area), m^2 (ft^2)	117.0	(1259)
Disk area, percent of S_o	53	
Vent area, m^2 (ft^2)	1.1	(11.9)
Vent area, percent of S_o	0.5	
Gap area, m^2 (ft^2)	26.5	(285.1)
Gap area, percent of S_o	12	
Band area, m^2 (ft^2)	77.2	(831.5)
Band area, percent of S_o	35	
Total geometric porosity, percent of S_o	12.5	
Suspension line length, m (ft)	16.8	(55)
Attachment riser length, m (ft)	2.7	(9)

TABLE IV.- PARACHUTE MATERIAL PROPERTIES

A. Nomex cloth used at parachute center disk area (plain weave, 200 denier yarn):		
Unit mass	99 g/m^2	(2.92 oz/yd^2)
Tensile strength (average of five measurements, ravel strip method):		
Warp direction	22 539 N/m	(128.7 lbf/in.)
Fill direction	21 821 N/m	(124.6 lbf/in.)
Maximum elongation (average of five measurements):		
Warp direction		25.7 percent
Fill direction		30 percent
Air permeability at differential pressure of 1.27 cm (0.5 in.) of H_2O	54.90 m^3/m^2/min	(180 ft^3/ft^2/min)
B. Dacron cloth used at parachute outer disk-edge area (dobbie weave):		
Unit mass	88 g/m^2	(2.6 oz/yd^2)
Tensile strength (average of five measurements, ravel strip method):		
Warp direction	15 937 N/m	(91 lbf/in.)
Fill direction	15 586 N/m	(89 lbf/in.)
Maximum elongation (average of five measurements):		
Warp direction		38.6 percent
Fill direction		48.9 percent
Air permeability at differential pressure of 1.27 cm (0.5 in.) of H_2O	23.79 m^3/m^2/min	(78 ft^3/ft^2/min)
C. Dacron cloth used in band area (rip-stop weave):		
Unit mass	69 g/m^2	(2.04 oz/yd^2)
Tensile strength (average of five measurements, ravel strip method):		
Warp direction	12 399 N/m	(70.8 lbf/in.)
Fill direction	12 504 N/m	(71.4 lbf/in.)
Maximum elongation (average of five measurements):		
Warp direction		37.3 percent
Fill direction		49.0 percent
Air permeability at differential pressure of 1.27 cm (0.5 in.) of H_2O	55.82 m^3/m^2/min	(183 ft^3/ft^2/min)
D. Radial and vent tapes (type 52 high-tenacity Dacron):		
Width	2.57 cm	(1.03 in.)
Thickness	0.017 cm	(0.066 in.)
Unit mass	29.8 g/m	(0.96 oz/yd)
Tensile strength	9275 N	(2085 lbf)
E. Hem tapes (type 52 high-tenacity Dacron):		
Width	2.65 cm	(1.01 in.)
Thickness	0.086 cm	(0.034 in.)
Unit mass	17.9 g/m	(0.576 oz/yd)
Tensile strength	4826 N	(1085 lbf)
F. Reinforcement tapes (type 52 high-tenacity Dacron):		
Width	1.91 cm	(0.75 in.)
Thickness	0.068 cm	(0.027 in.)
Unit mass	8.6 g/m	(0.277 oz/yd)
Tensile strength	2600 N	(585 lbf)
G. Suspension lines (type 52 high-tenacity Dacron):		
Unit mass	19.1 g/m	(0.615 oz/yd)
Maximum elongation		21 percent
Tensile strength (average of five measurements)	9785 N	(2200 lbf)
H. Riser webbing (Dacron):		
Width	4.45 cm	(1.75 in.)
Thickness	0.55 cm	(0.217 in.)
Unit mass	211 g/m	(6.8 oz/yd)
Maximum elongation		9.5 percent
Tensile strength (average of five measurements)	100 500 N	(22 570 lbf)

TABLE V.- PARACHUTE SYSTEM MASSES

	kg	lbm	kg	lbm
Parachute, packed, including canopy, suspension lines, bridle, and deployment bag (measured)			55.93	123.3
Canopy:				
Nomex cloth, disk area (estimated)	6.26	13.79		
Dacron cloth, disk area (estimated)	6.84	15.09		
Dacron cloth, band area (estimated)	6.22	13.71		
Radial tapes (estimated)	11.62	25.61		
Hem tapes (estimated)	2.19	4.82		
Rip-stop reinforcement tapes (estimated)	0.21	0.46		
Suspension lines (estimated)	14.08	31.04		
Risers, including links (estimated)	6.69	14.76		
Deployment bag (measured)	0.91	2.0		
Miscellaneous thread, ink, etc. (estimated)	0.91	2.0		
Mortar cover (measured)			1.13	2.5
Total weight of system (measured)			57.1	125.8

TABLE VI.- PARACHUTE DAMAGE IDENTIFICATION CHART

Time, t', sec	Disk-area damage, gore no.	Band-area damage, gore no.
1.19	2, 4, 10	
1.21	23	
1.23	26	
1.26	33	33, 34, 35
1.27	17, 18	
1.29	22	
1.35	1, 41	
1.37	6, 37	
1.38	35	
1.40	3, 5	
1.50	24, 36	
1.56		21
1.83		3, 39, 41
1.85	7, 9	32
1.86	8	26, 37
1.89	42	19, 23, 24, 25
1.91		9
1.93	25, 38	13
2.10	34	27
2.87		1, 2, 4
2.91	20	
3.47	32	

TABLE VII.- TRAJECTORY DATA USED FOR STAGNATION-LINE TEMPERATURE CALCULATIONS

Time, t', sec	Altitude		Velocity, V_∞		Density, ρ_∞		Temperature, T_∞		Speed of sound, a_∞	
	km	ft	m/sec	ft/sec	kg/m^3	$slugs/ft^3$	K	^oR	m/sec	ft/sec
[a]1.2	42.79	140.38×10^3	871	2859	2.72×10^{-3}	5.27×10^{-6}	269	485	329	1079
1.6	42.47	139.35	854	2803	2.84	5.51	268	483	328	1077
2.0	42.17	138.34	837	2746	2.96	5.75	267	481	328	1075
2.5	41.79	137.11	816	2676	3.12	6.06	266	479	327	1073
3.0	41.43	135.91	794	2605	3.28	6.36	265	477	326	1071
3.5	41.07	134.74	772	2534	3.45	6.70	264	475	326	1069
4.0	40.72	133.60	751	2464	3.61	7.00	263	473	325	1066
4.5	40.38	132.49	730	2394	3.79	7.35	262	471	324	1064

[a]Parachute is first open at approximately 1.2 sec after mortar firing.

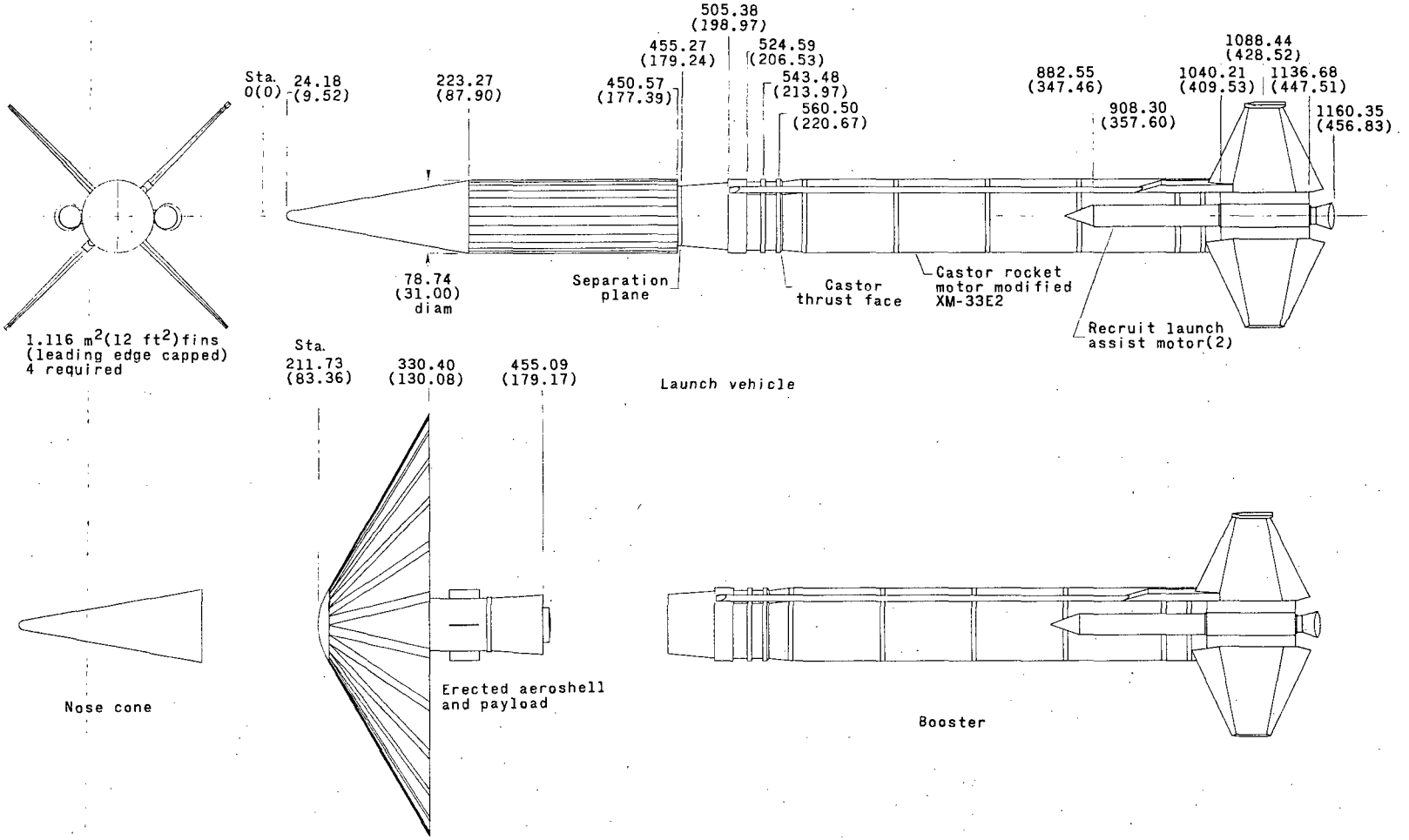

Figure 1.- Sketch of launch vehicle and separated parts including erected aeroshell and payload. All station numbers and dimensions are in cm (in.).

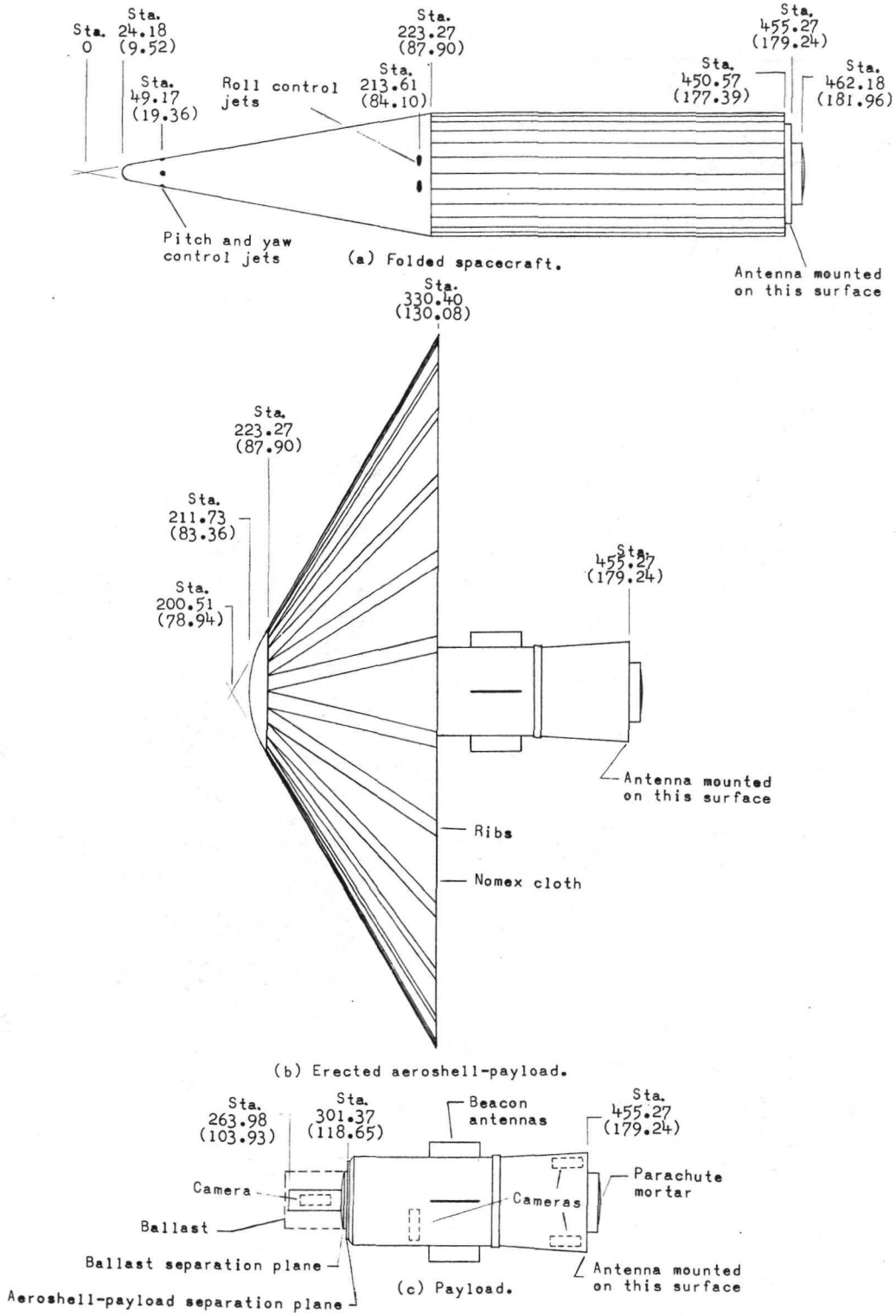

Figure 2.- Sketches of folded aeroshell, erected aeroshell-payload combination, and payload alone. All station numbers are in cm (in.).

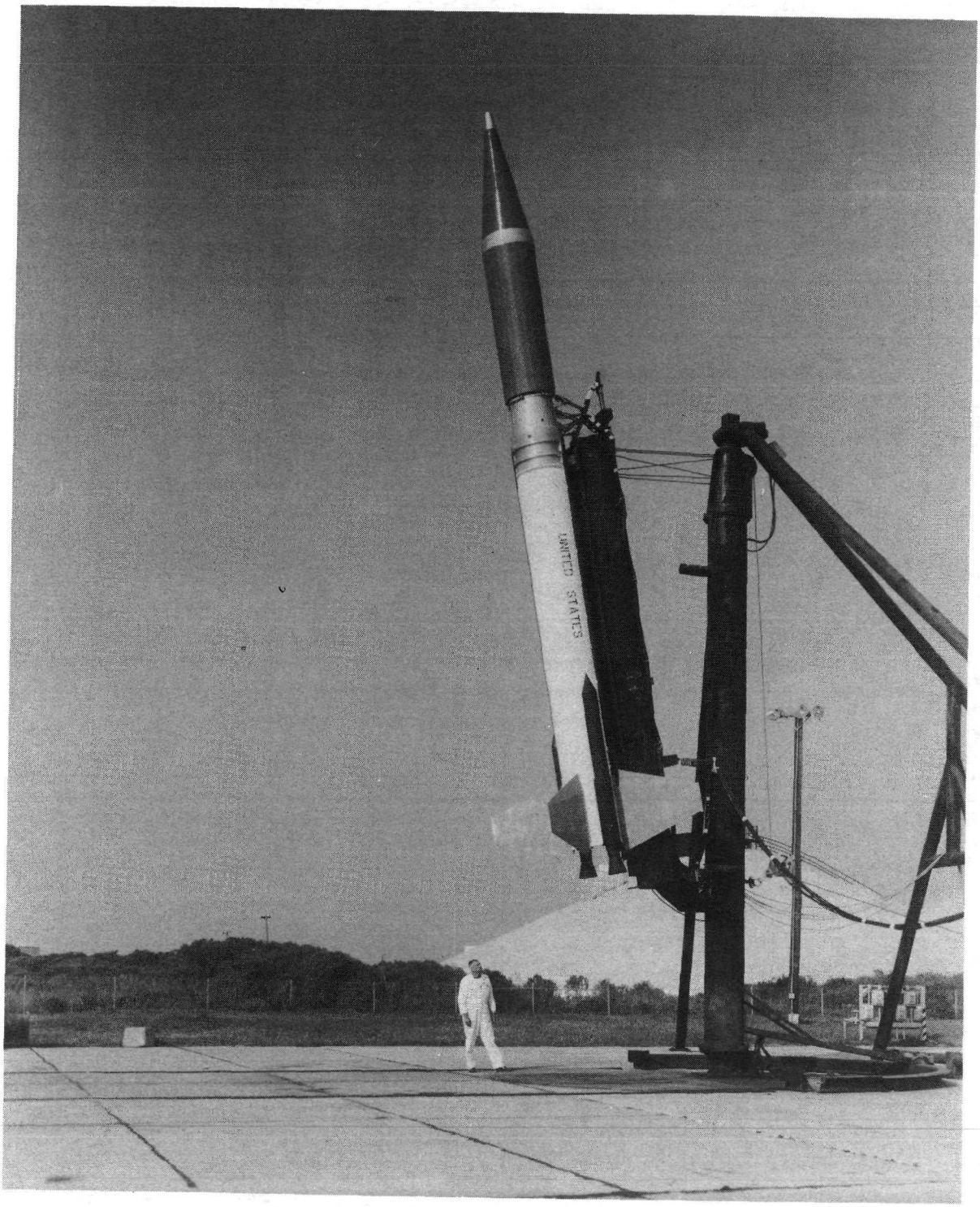

L-70-258

Figure 3.- Test vehicle on launcher.

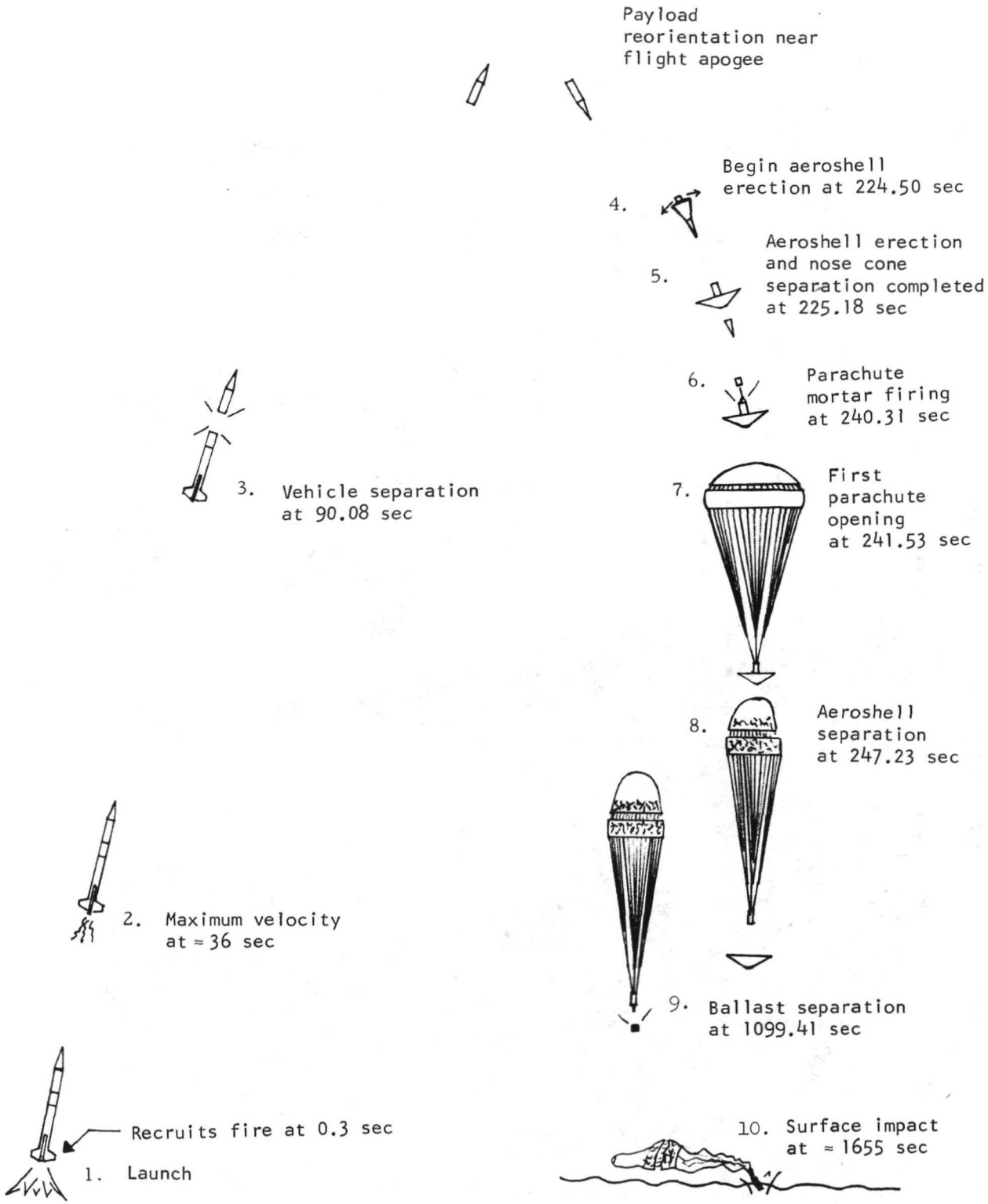

Figure 4.- Flight sequence of events.

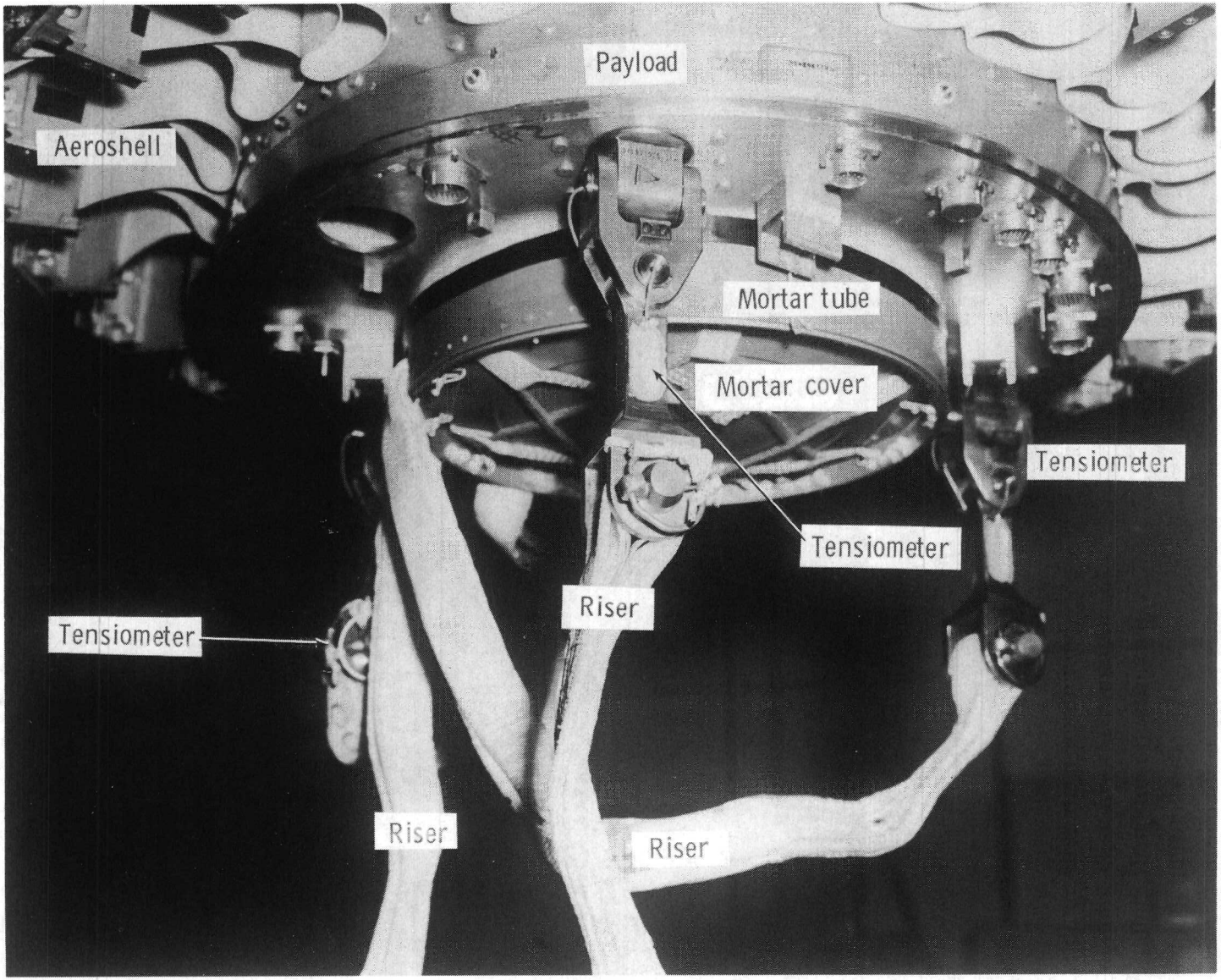

L-70-24.1

Figure 5.- Photograph of aft end of payload showing tensiometers, risers, end of mortar tube, and mortar cover.

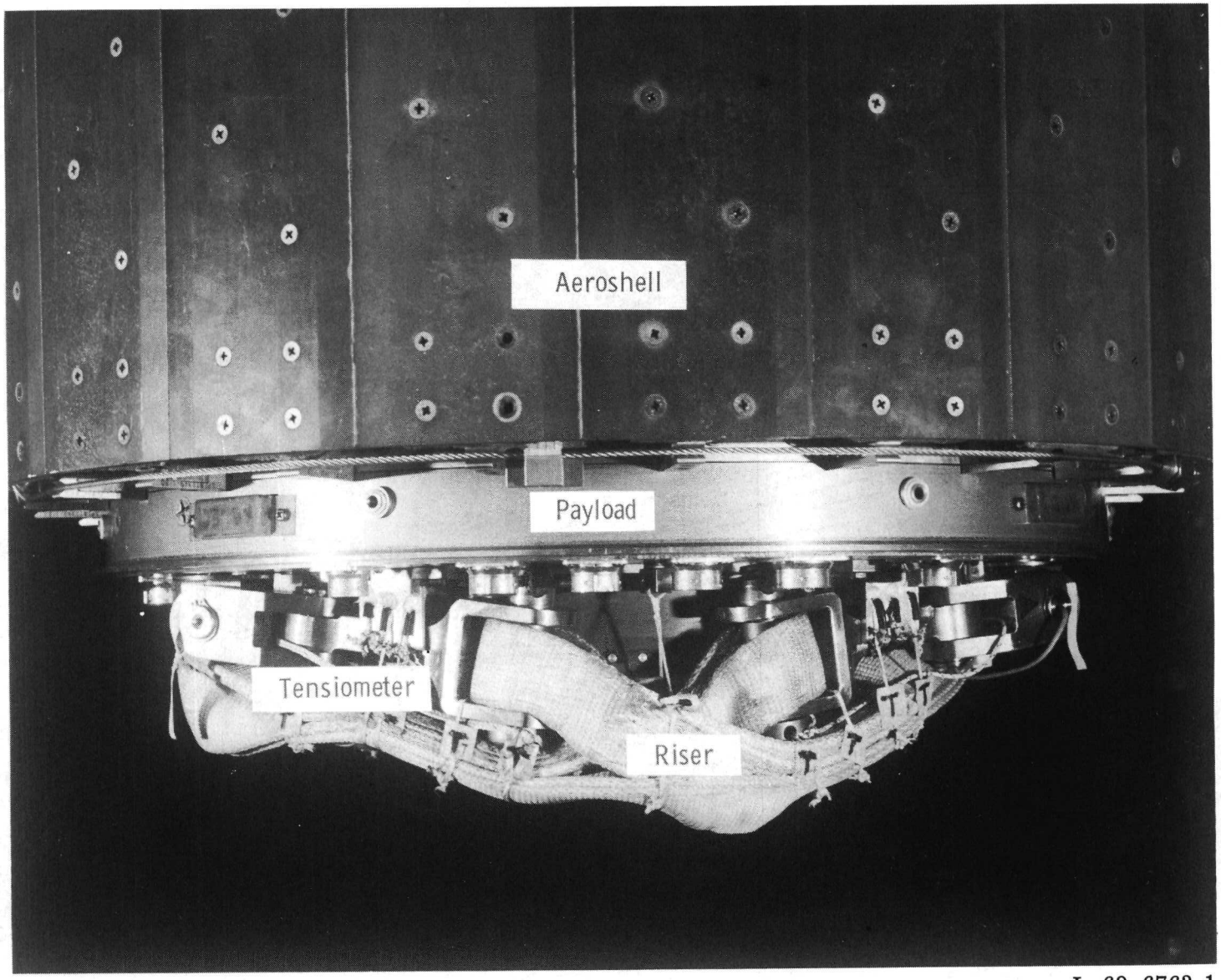

L-69-6763.1

Figure 6.- Photograph of aft end of payload showing method of stowing tensiometers and risers.

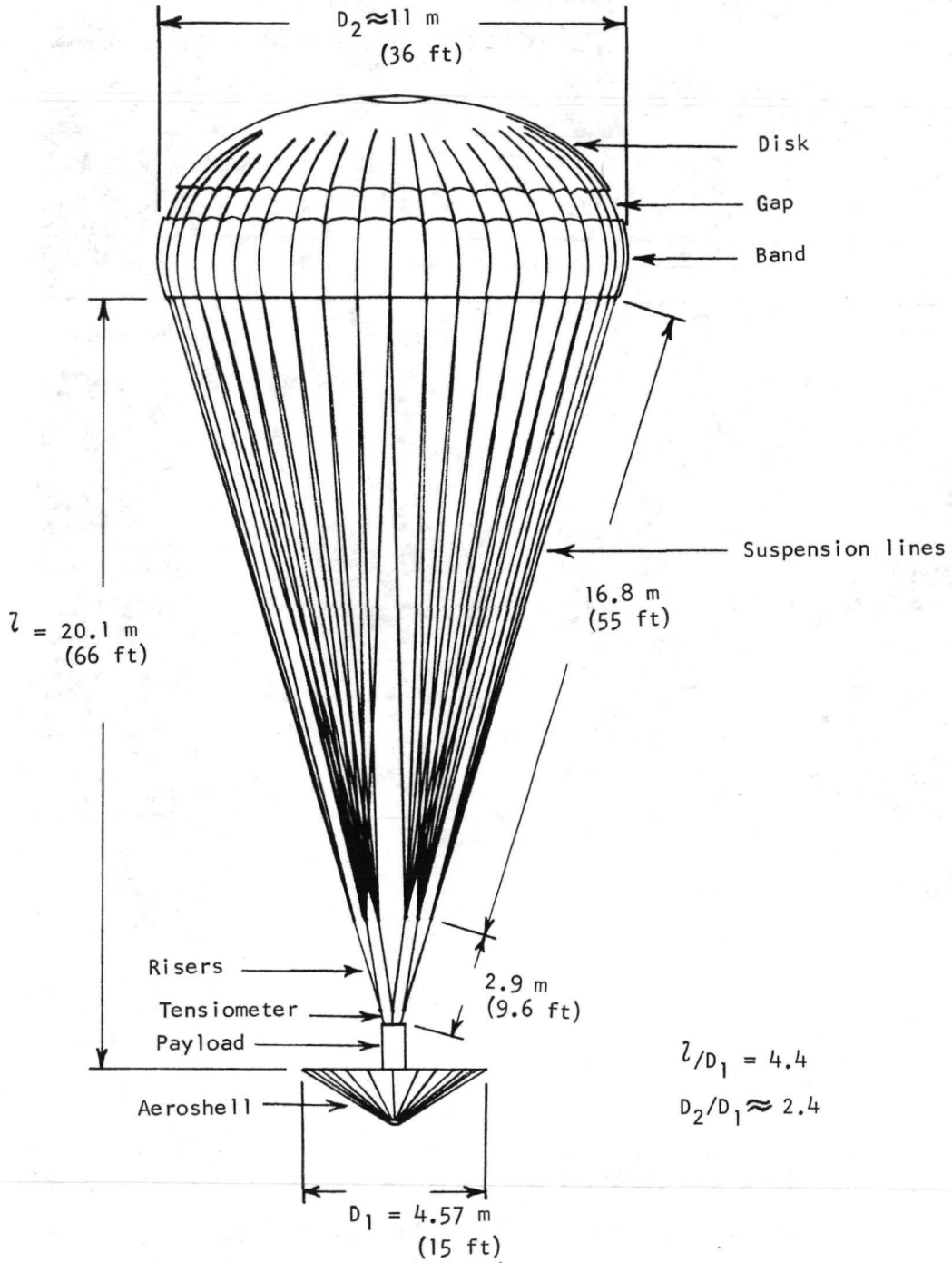

Figure 7.- Sketch of parachute and aeroshell-payload configuration.

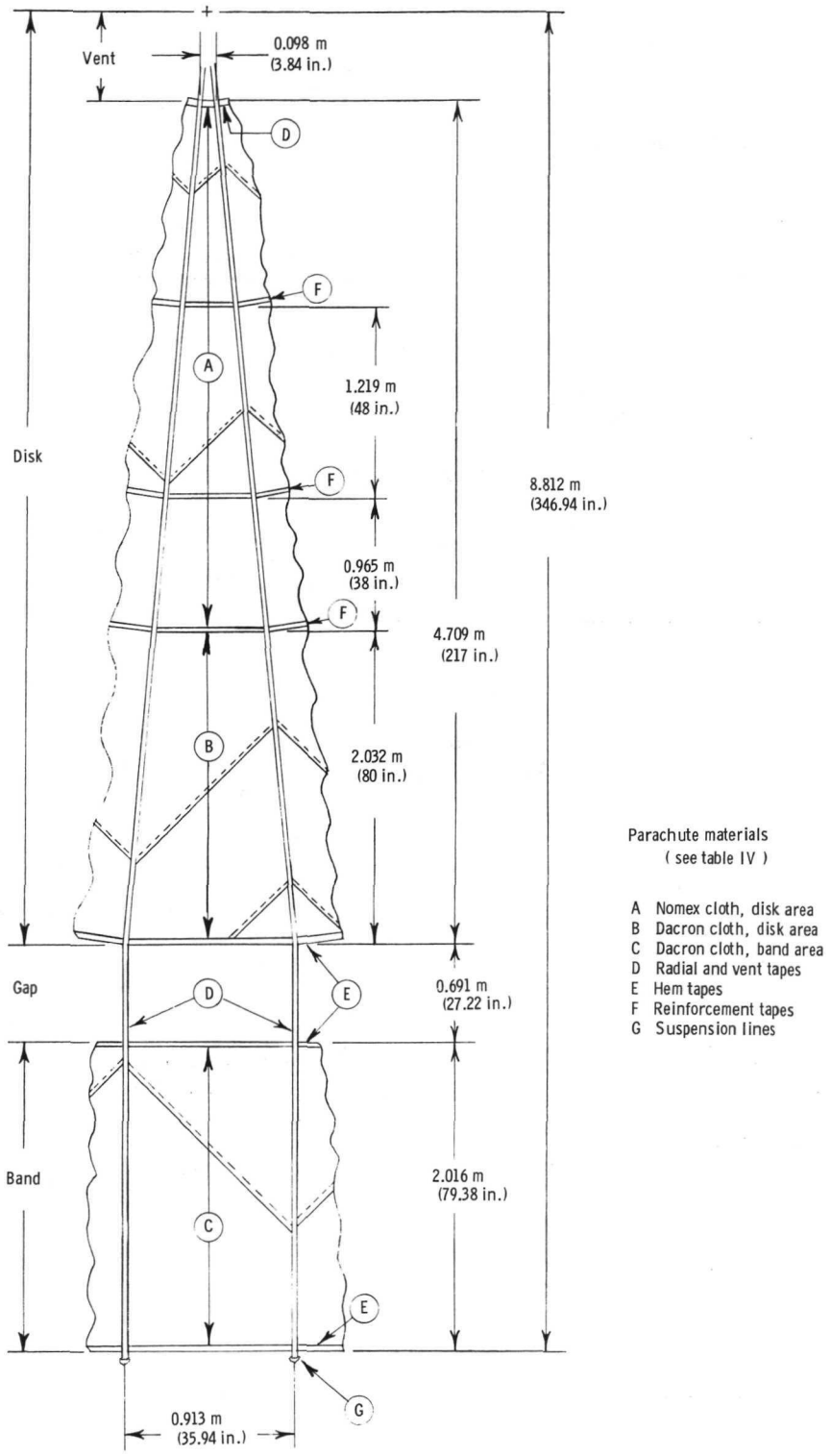

Figure 8.- Parachute gore details.

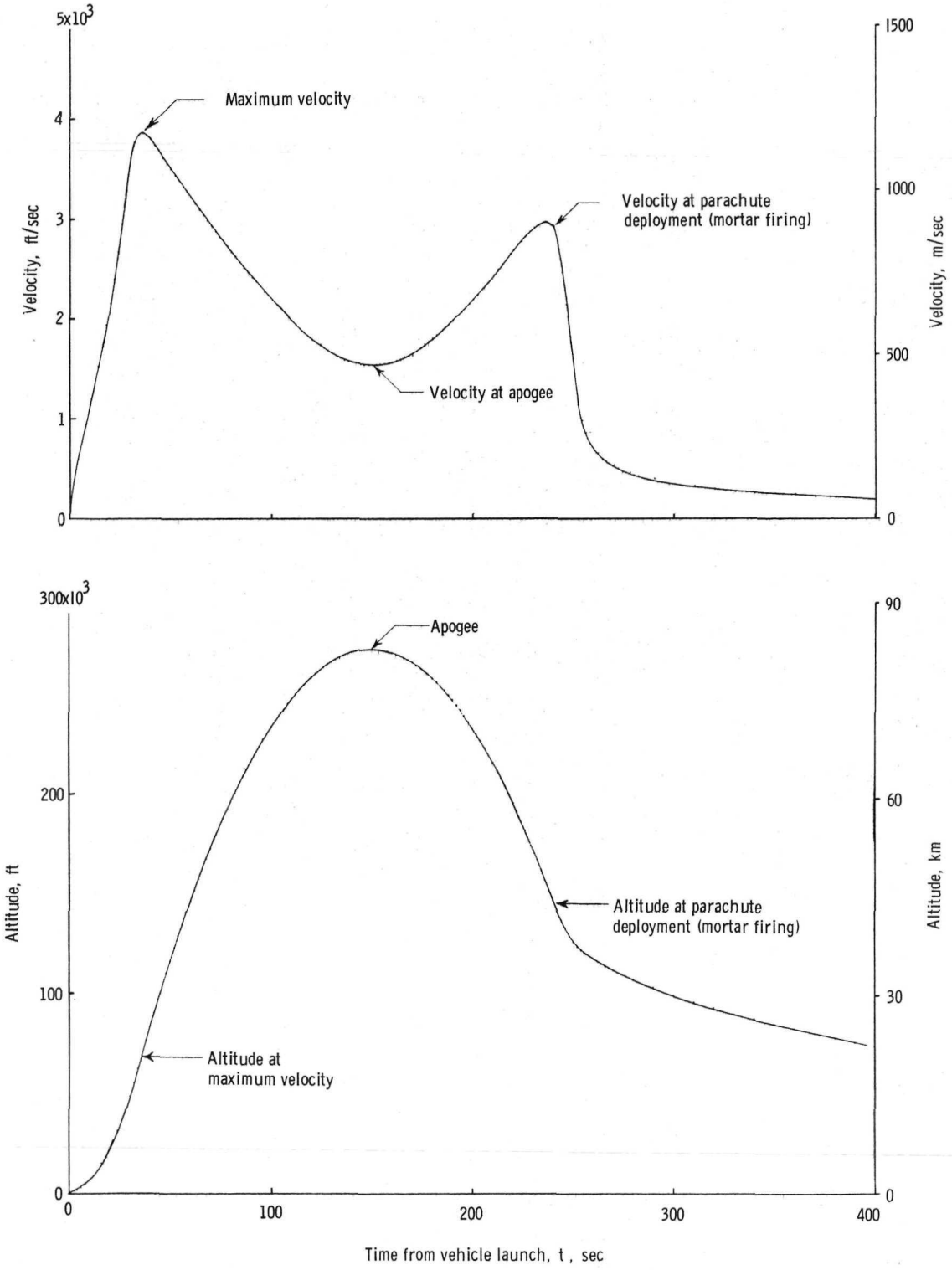

Figure 9.- Flight history of altitude and relative velocity.

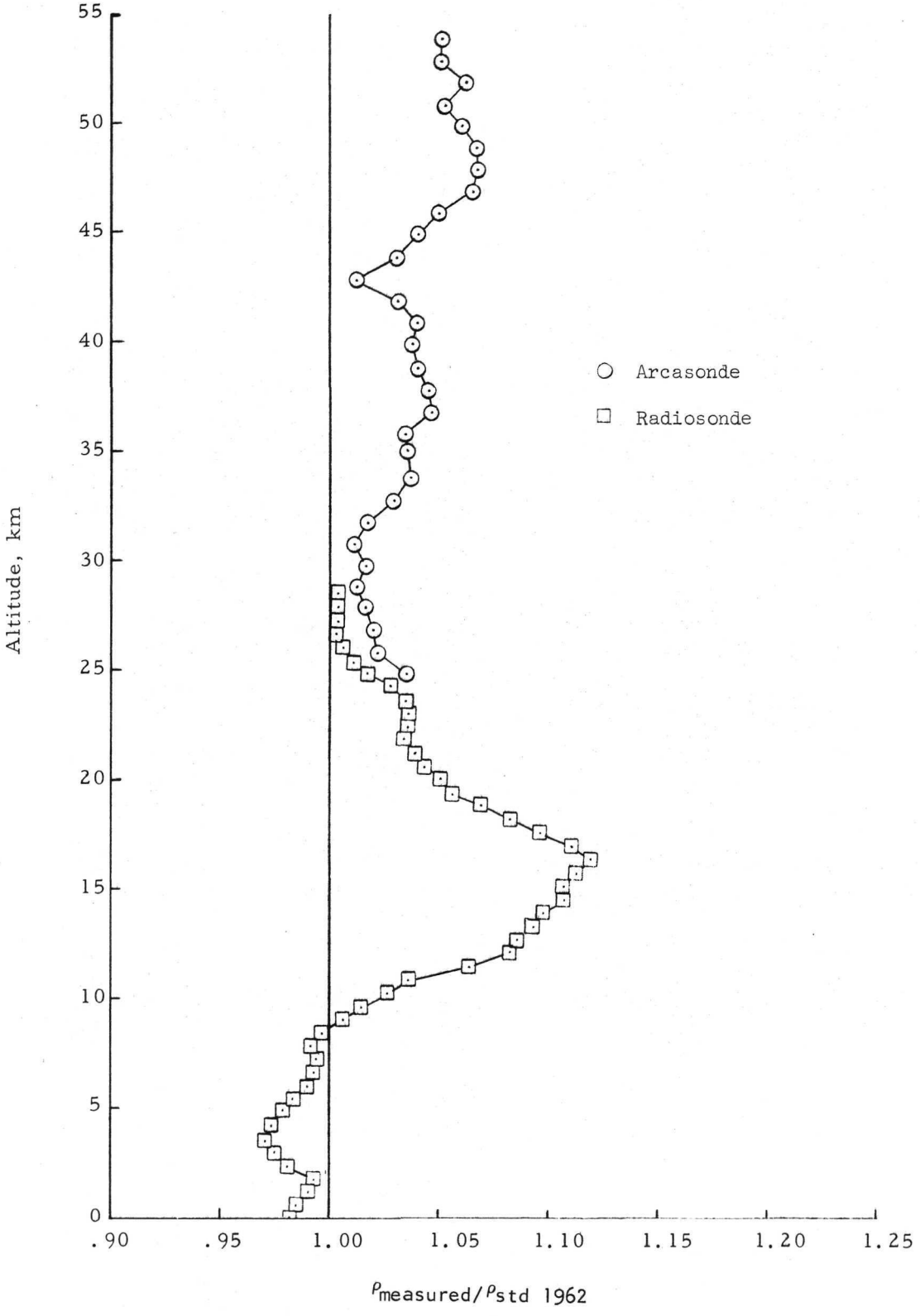

Figure 10.- Atmospheric-density profile.

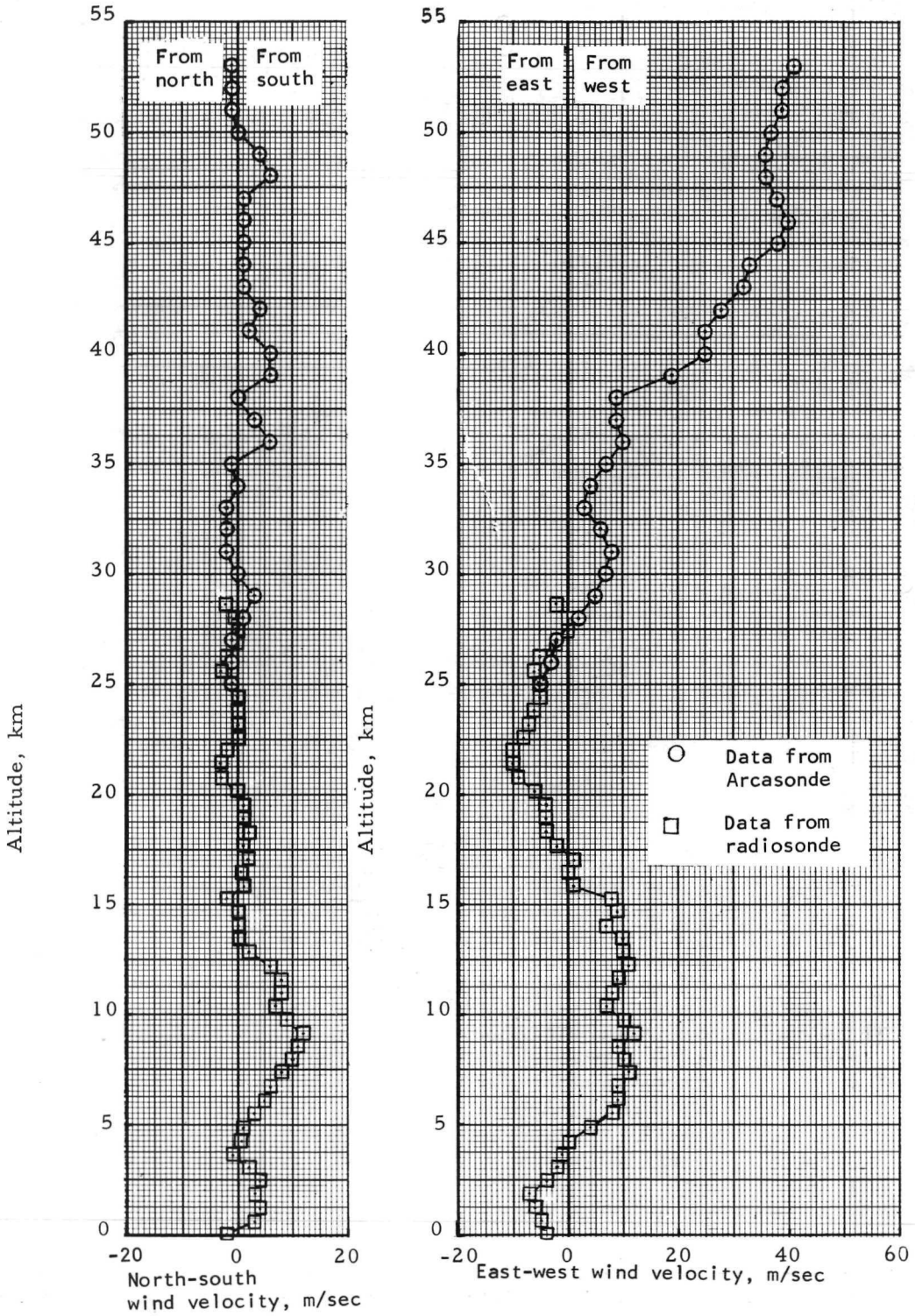

Figure 11.- Wind-velocity profile in north-south and east-west components.

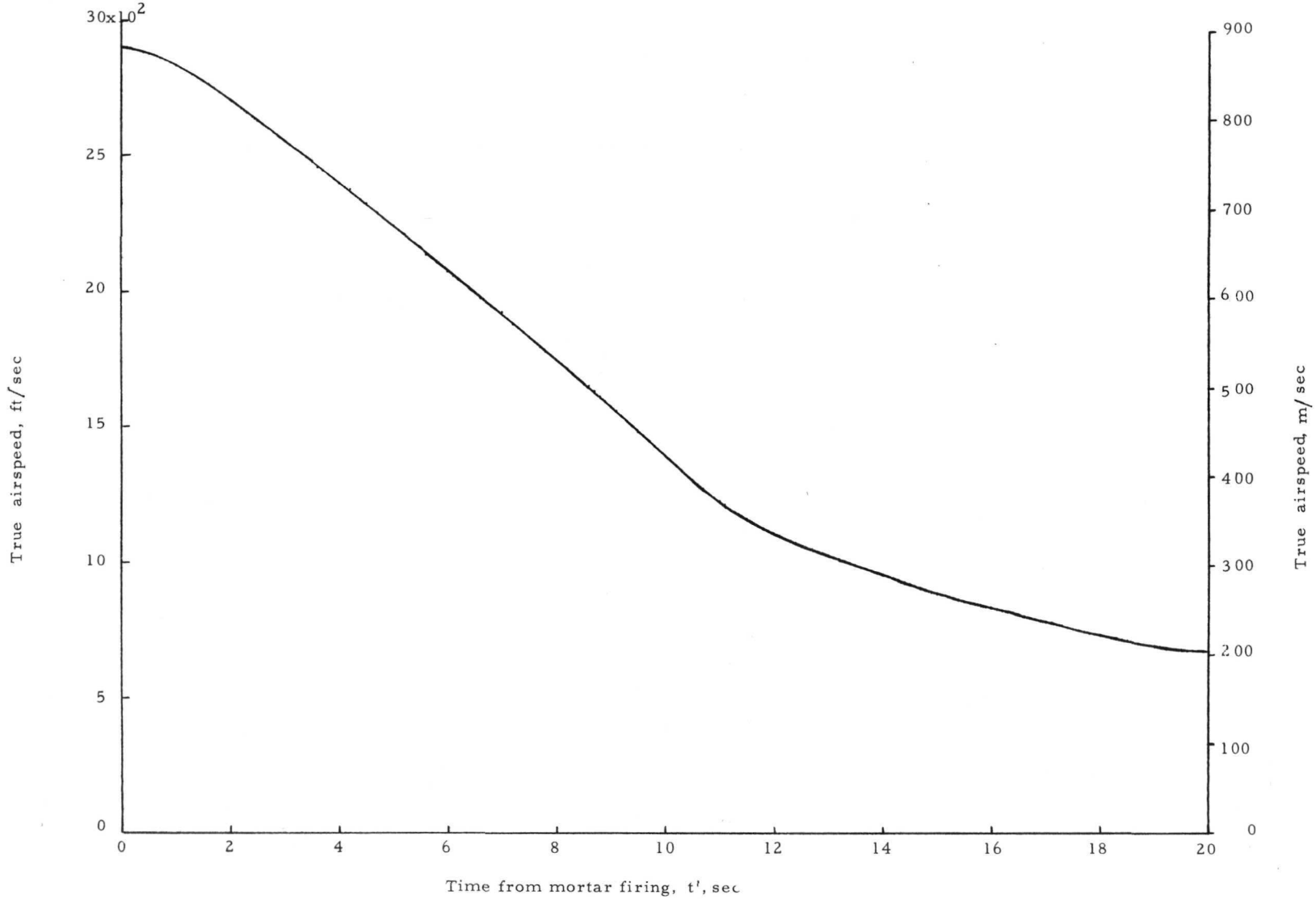

Figure 12.- True-airspeed history after mortar firing.

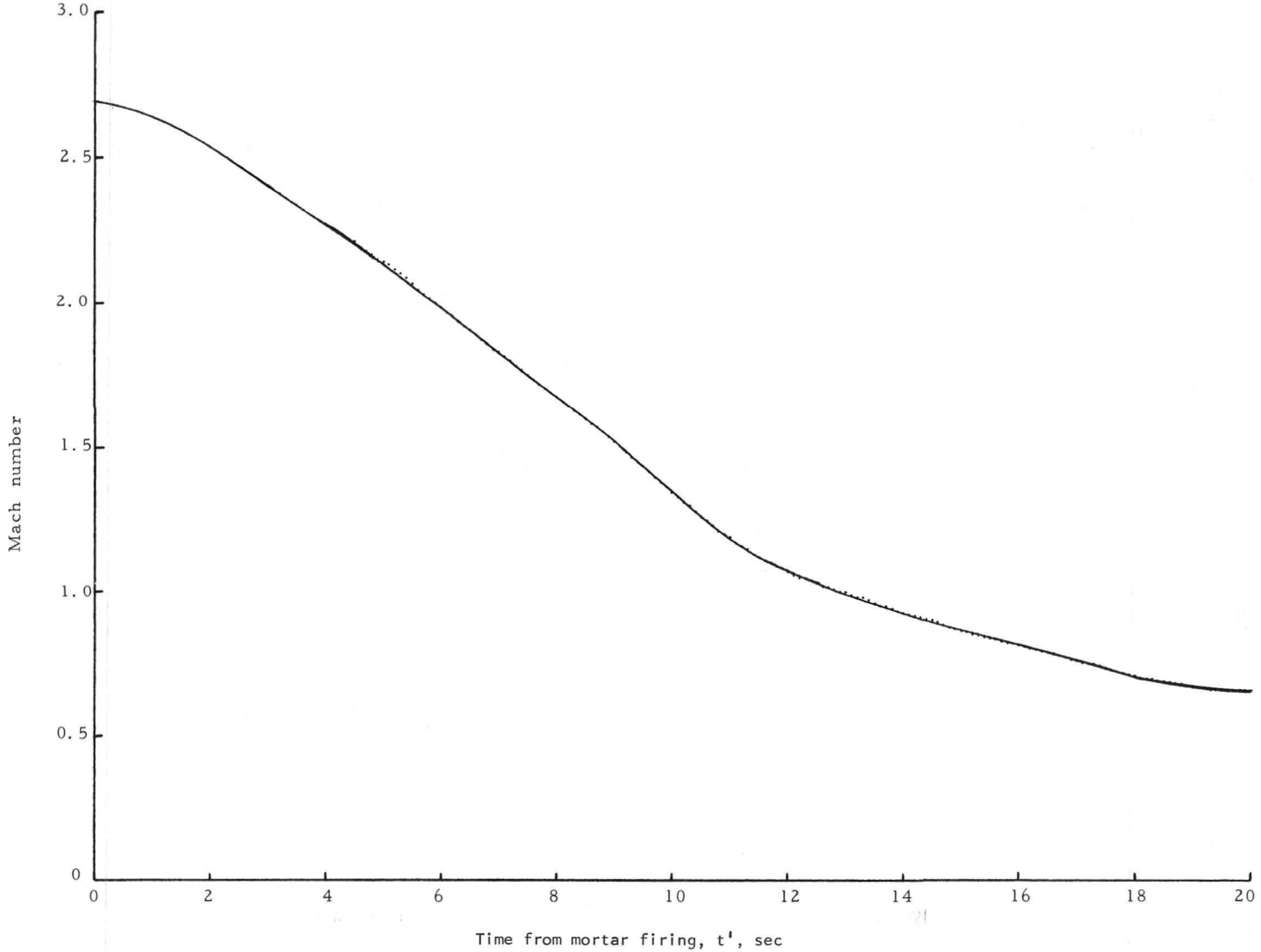

Figure 13.- Mach number history after mortar firing.

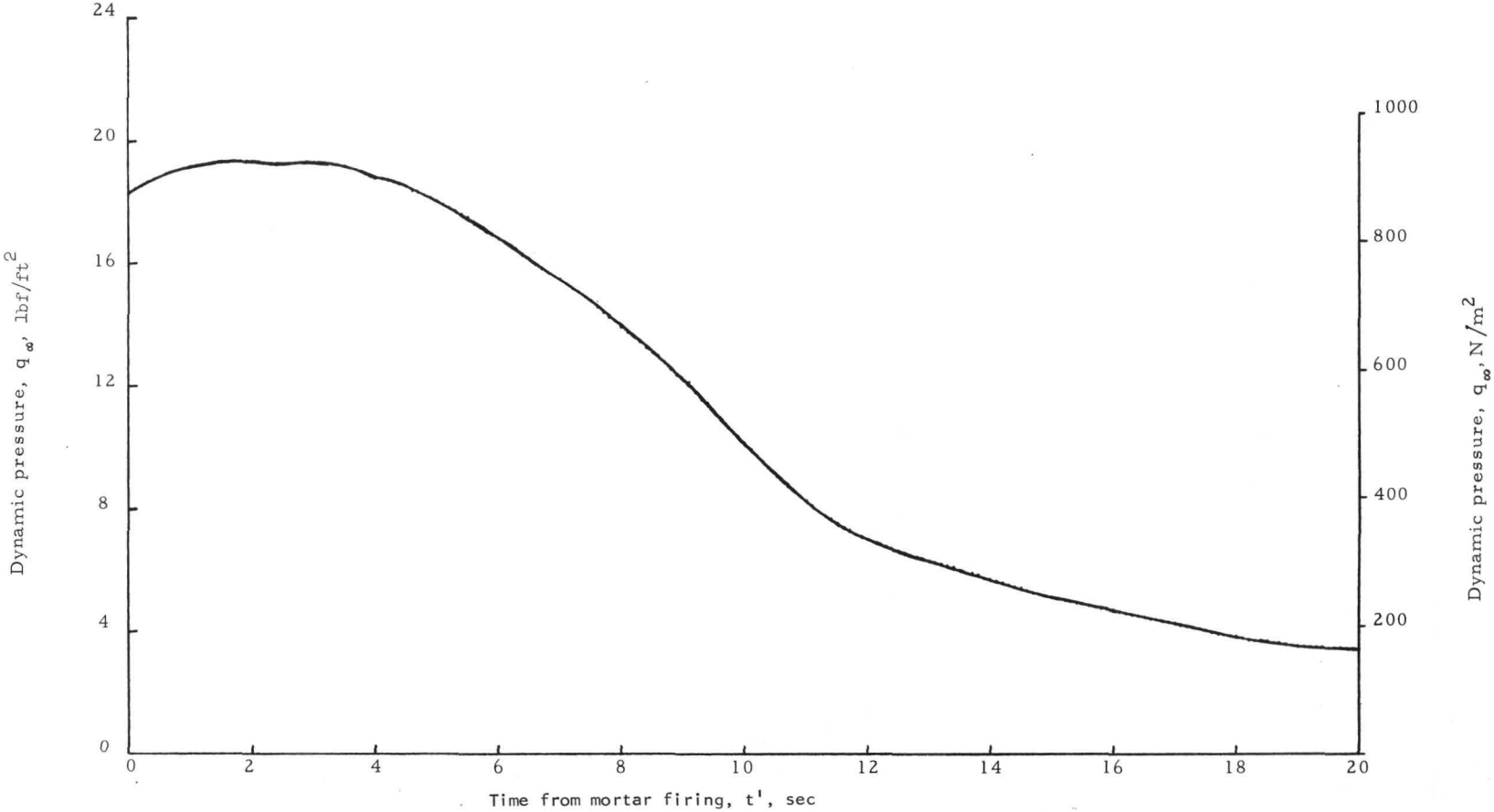

Figure 14.- Dynamic-pressure history after mortar firing.

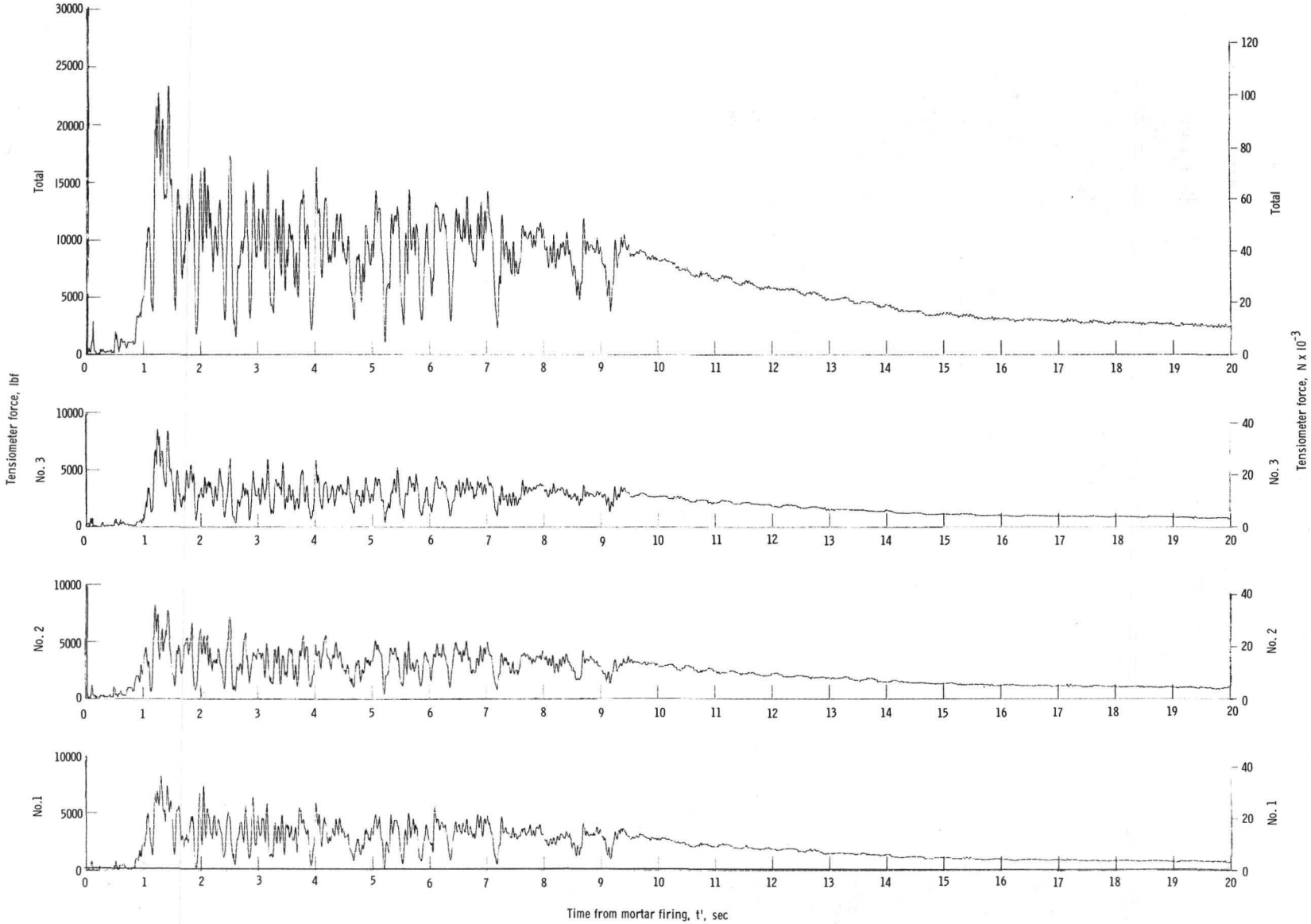

Figure 15.- Histories of measured tensiometer forces.

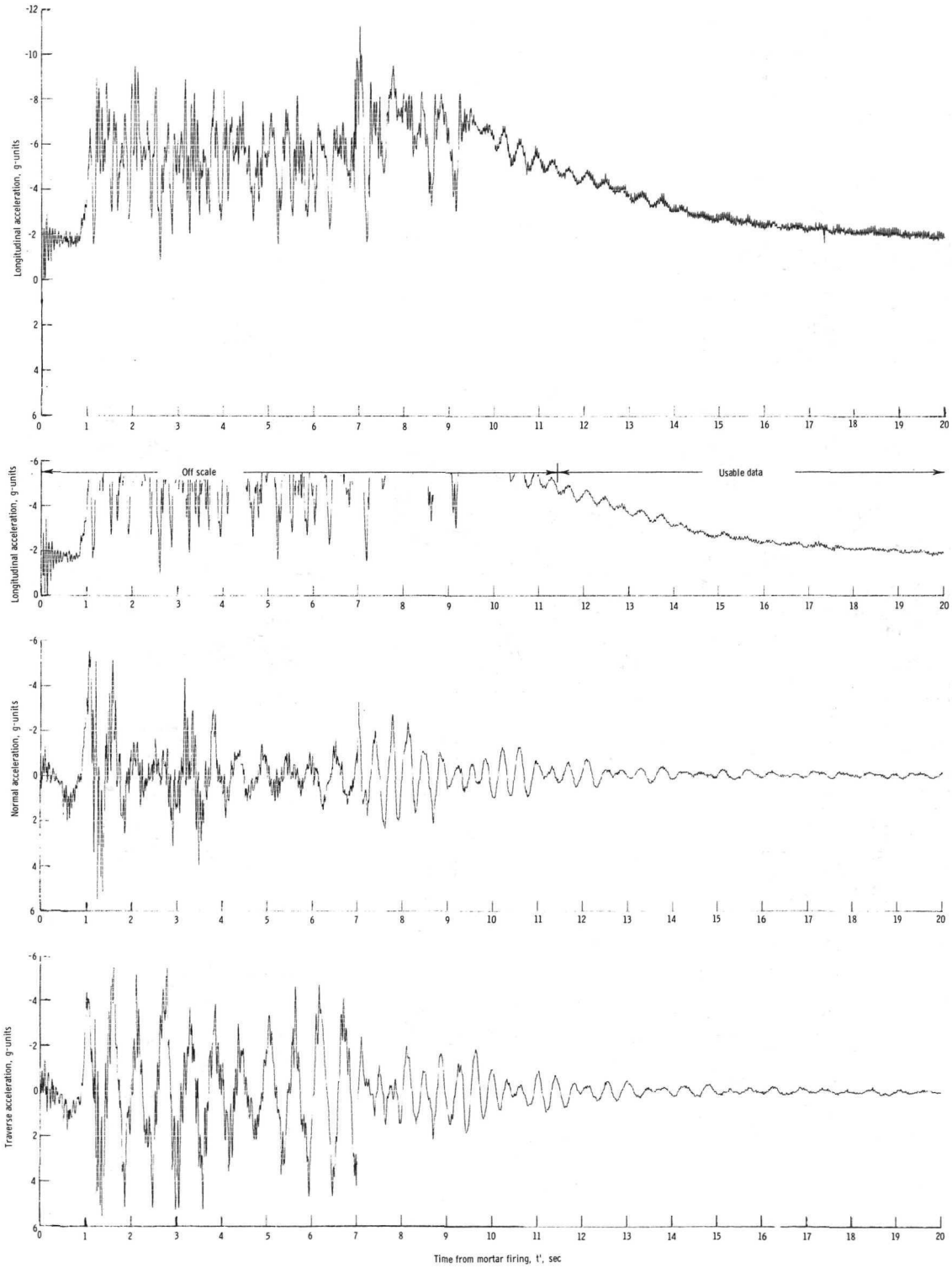

Figure 16.- Acceleration time histories.

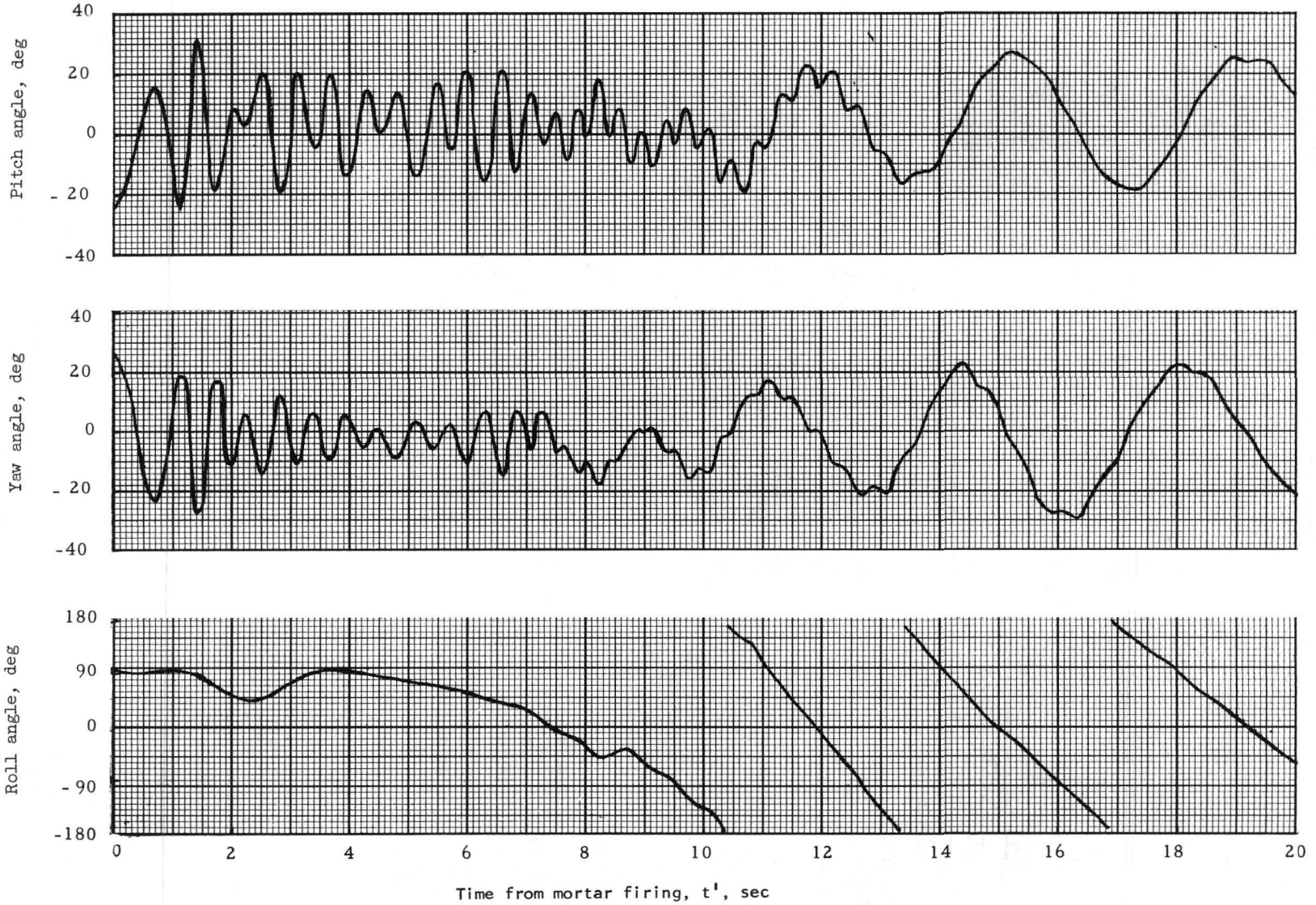

Figure 17.- Payload pitch, yaw, and roll angles with respect to vehicle flight path.

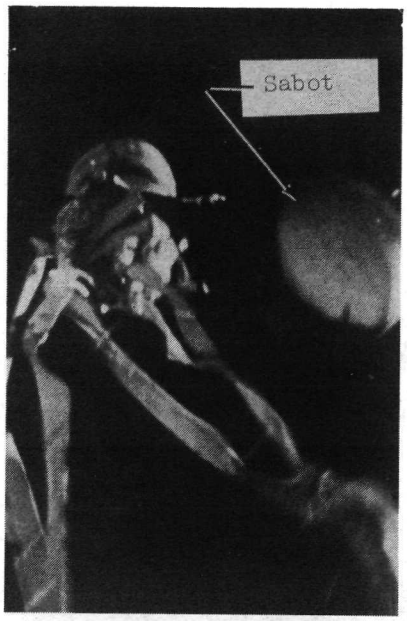

Frame 6, t' = 0.096 sec

Frame 7, t' = 0.111 sec

Frame 8, t' = 0.127 sec

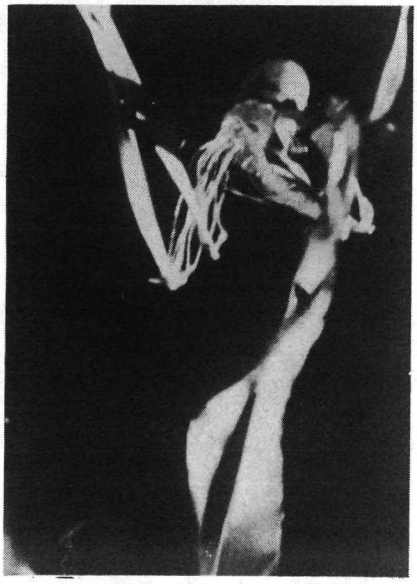

Frame 9, t' = 0.143 sec

L-72-6590

(a) Parachute pack ejection.

Figure 18.- Onboard camera photographs.

Frame 10, t' = 0.159 sec

Frame 11, t' = 0.175 sec

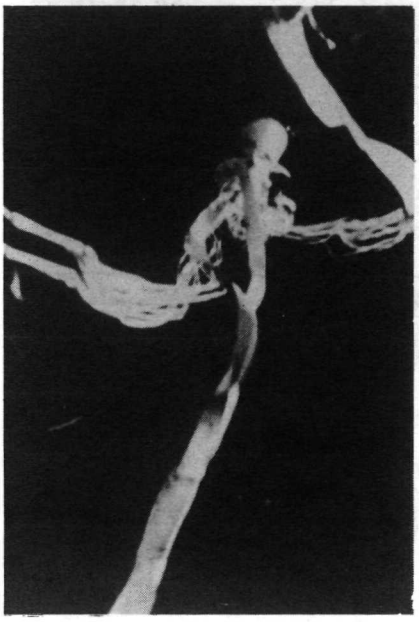

Frame 12, t' = 0.191 sec

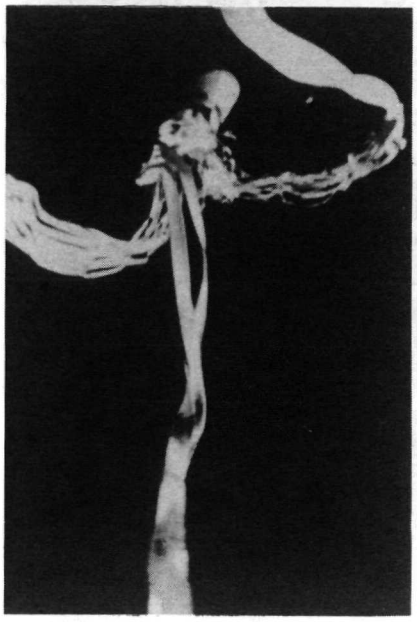

Frame 13, t' = 0.207 sec

L-72-6591

(a) Concluded.

Figure 18.- Continued.

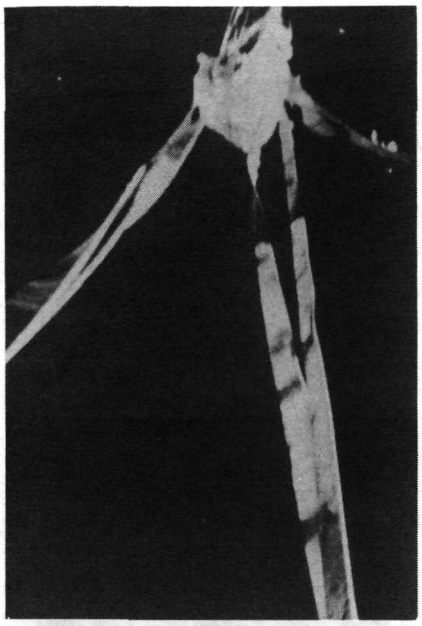

Frame 52, t' = 0.828 sec

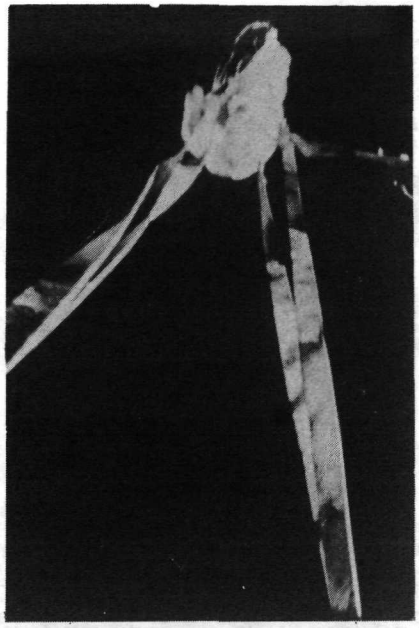

Frame 53, t' = 0.844 sec

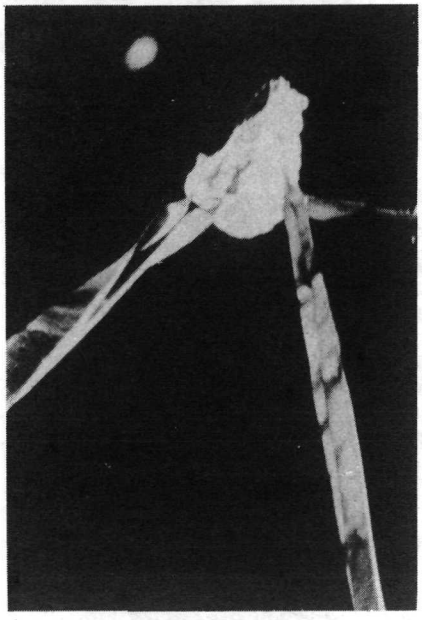

Frame 54, t' = 0.860 sec

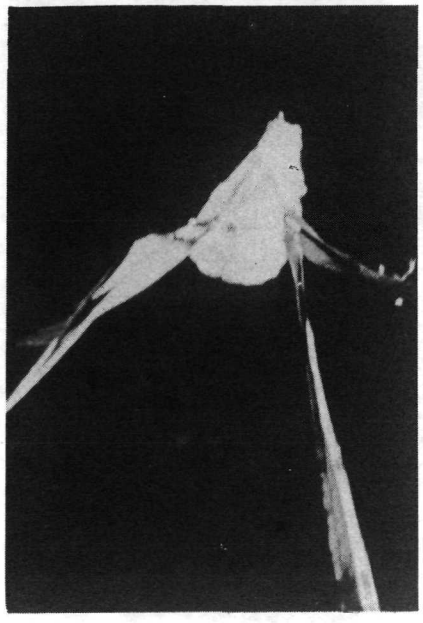

Frame 55, t' = 0.876 sec

L-72-6592

(b) Initial canopy deployment.

Figure 18.- Continued.

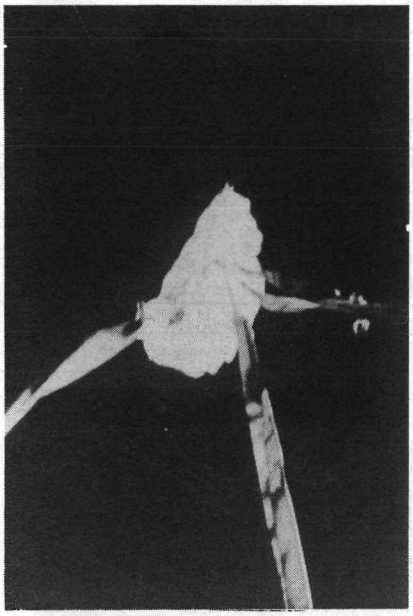

Frame 56, t' = 0.892 sec

Frame 57, t' = 0.908 sec

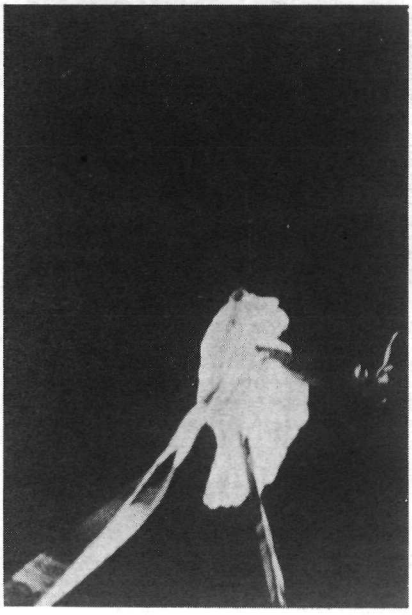

Frame 58, t' = 0.924 sec

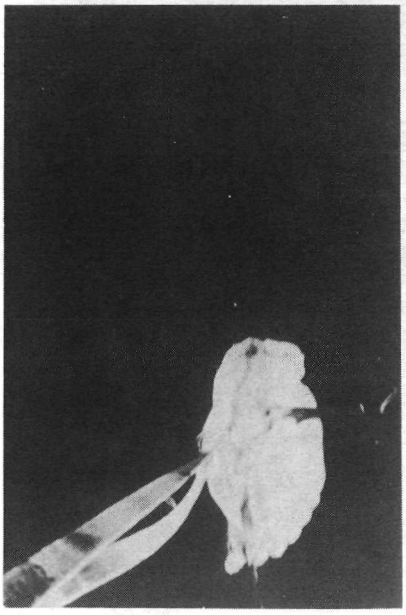

Frame 59, t' = 0.939 sec

L-72-6593

(b) Concluded.

Figure 18.- Continued.

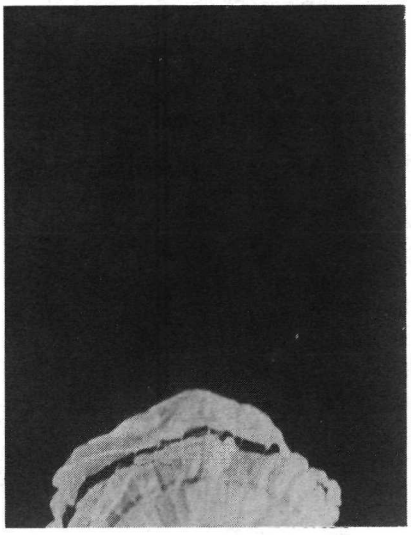

Frame 71, t' = 1.131 sec

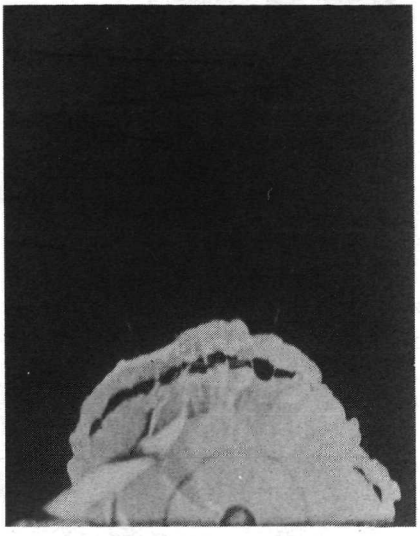

Frame 72, t' = 1.146 sec

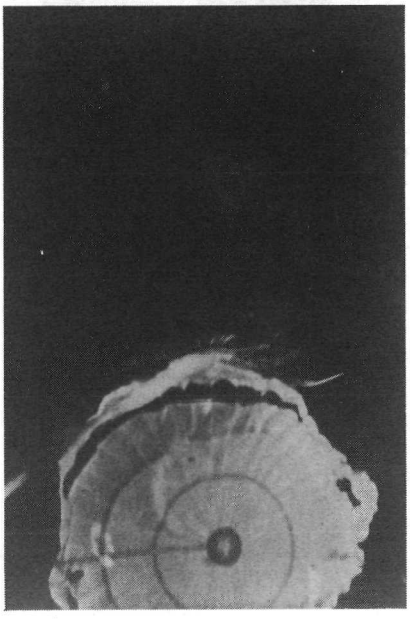

Frame 73, t' = 1.162 sec

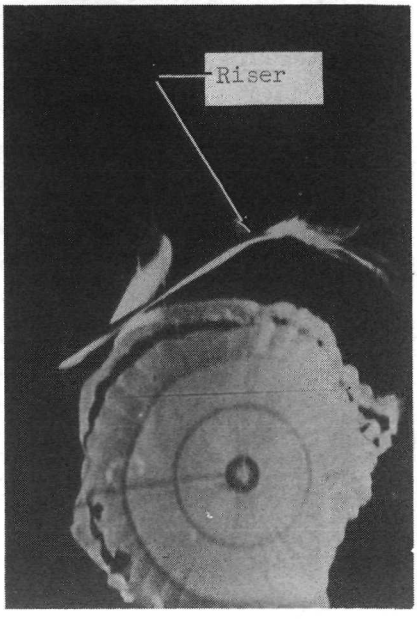

Frame 74, t' = 1.178 sec

L-72-6594

(c) First canopy inflation and damage identification series.

Figure 18.- Continued.

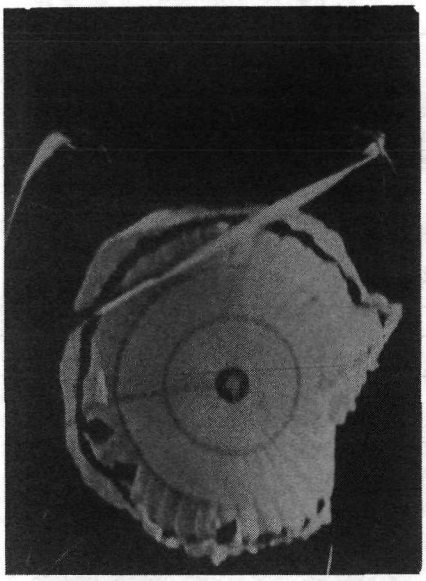

Frame 75, t' = 1.194 sec

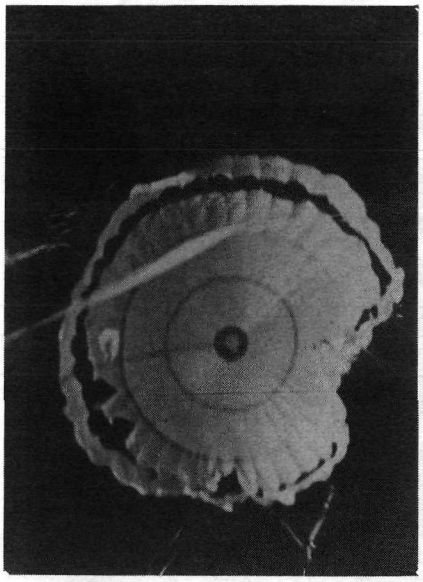

Frame 76, t' = 1.210 sec
(maximum frontal area)

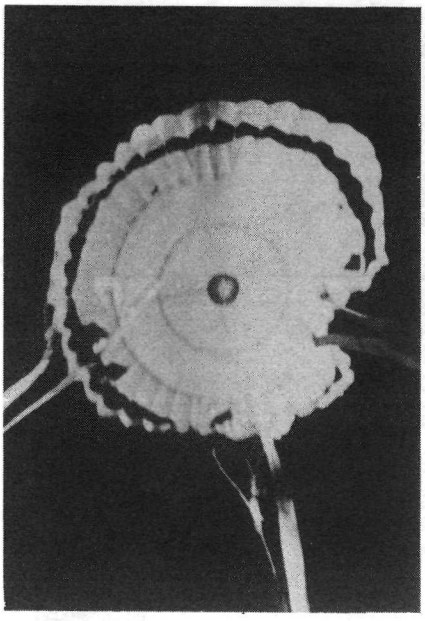

Frame 77, t' = 1.226 sec

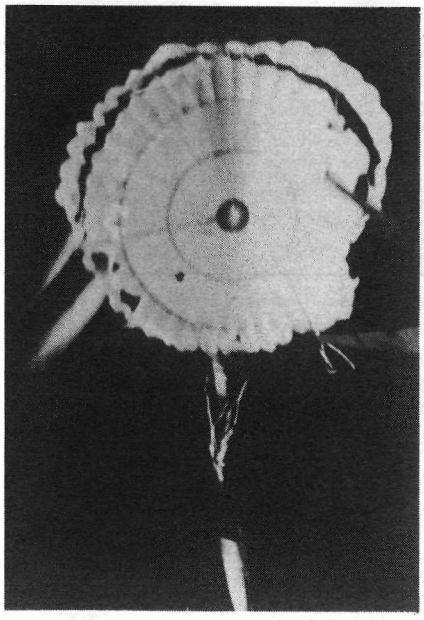

Frame 78, t' = 1.242 sec

L-72-6595

(c) Continued.

Figure 18.- Continued.

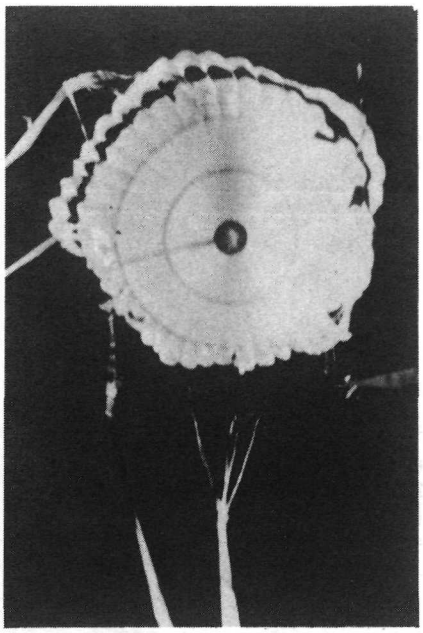

Frame 79, t' = 1.258 sec

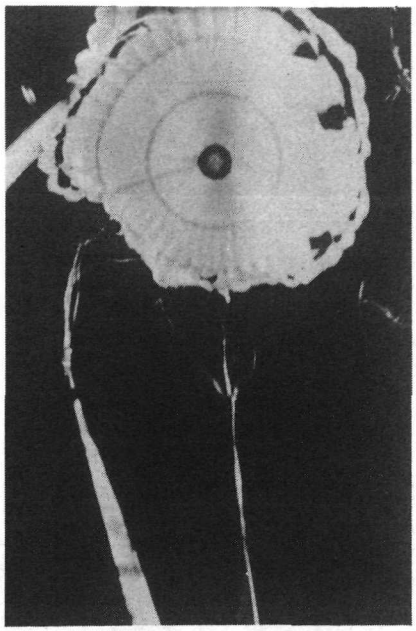

Frame 80, t' = 1.274 sec

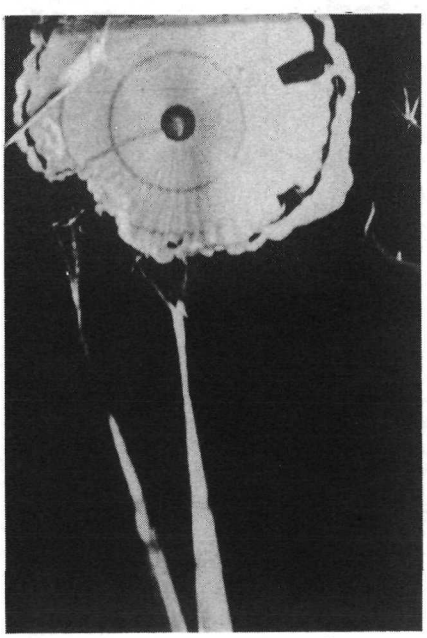

Frame 81, t' = 1.290 sec

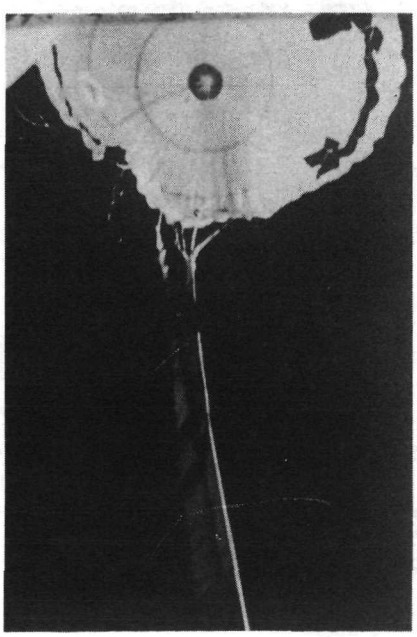

Frame 82, t' = 1.306 sec

L-72-6596

(c) Concluded.

Figure 18.- Continued.

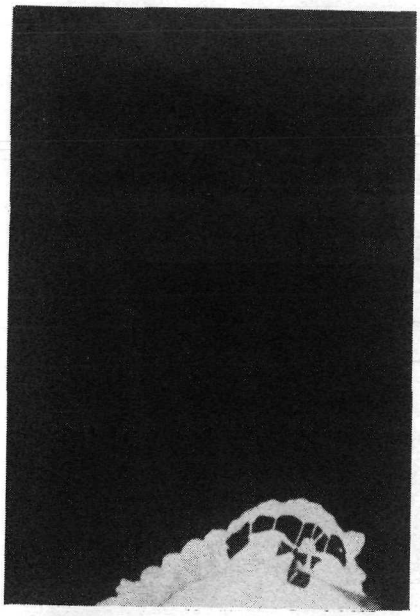

Frame 98, t' = 1.561 sec

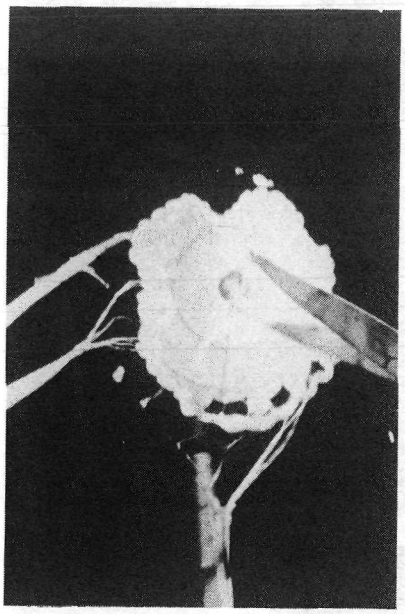

Frame 110, t' = 1.752 sec

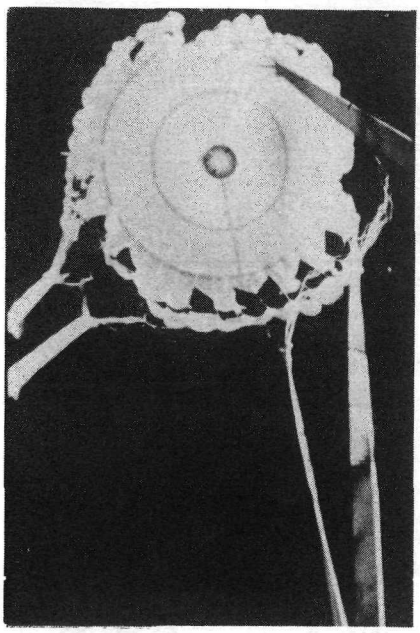

Frame 115, t' = 1.831 sec

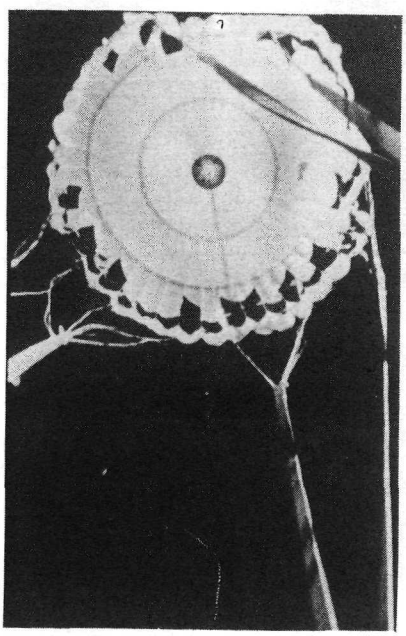

Frame 116, t' = 1.847 sec

L-72-6597

(d) Canopy frontal area variations and continued damage identification.

Figure 18.- Continued.

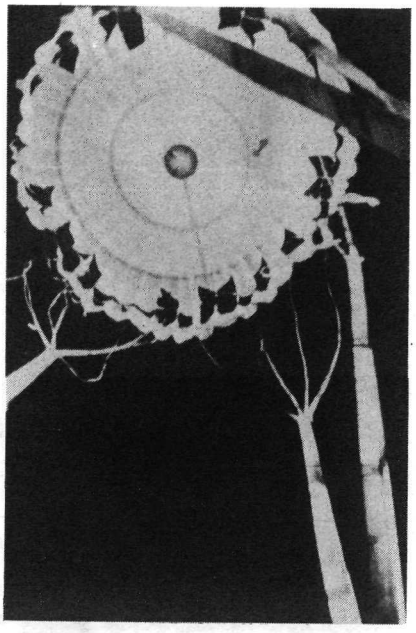

Frame 117, t' = 1.863 sec

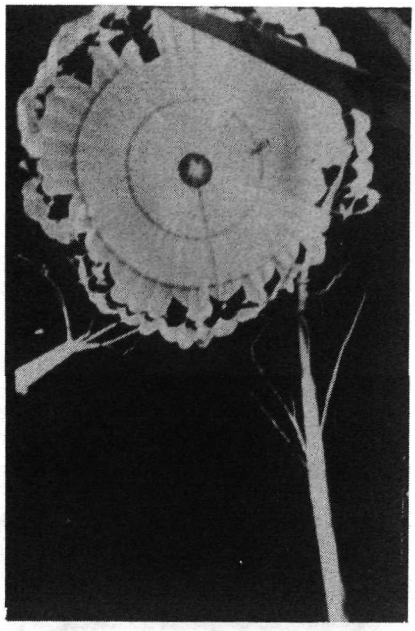

Frame 118, t' = 1.879 sec

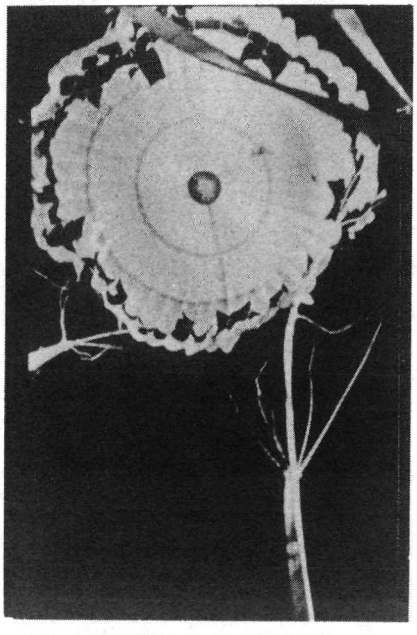

Frame 119, t' = 1.894 sec

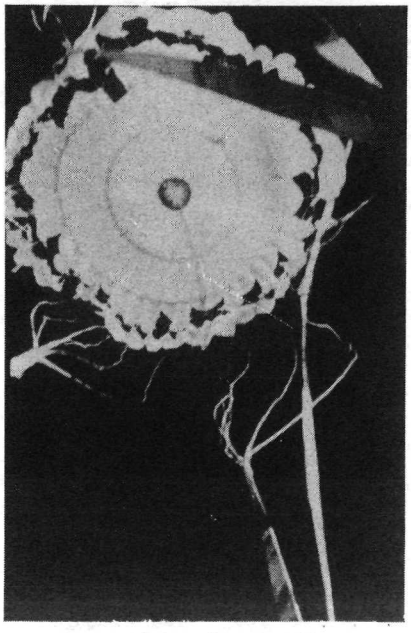

Frame 120, t' = 1.911 sec

L-72-6598

(d) Continued.

Figure 18.- Continued.

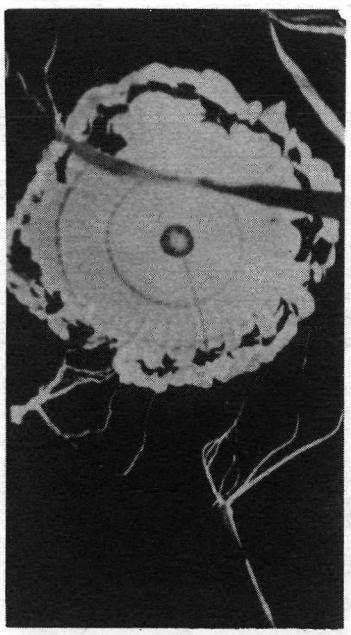

Frame 121, t' = 1.927 sec

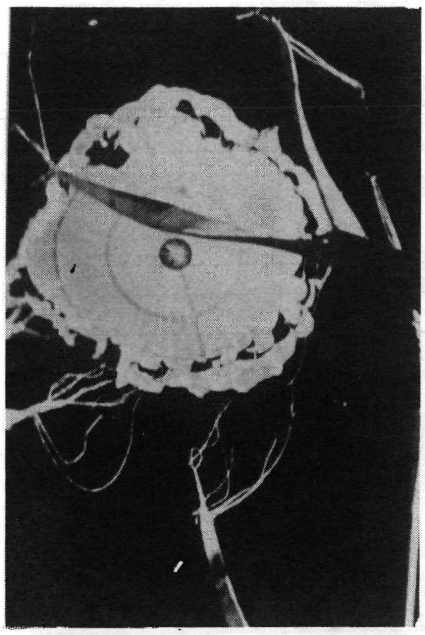

Frame 122, t' = 1.943 sec

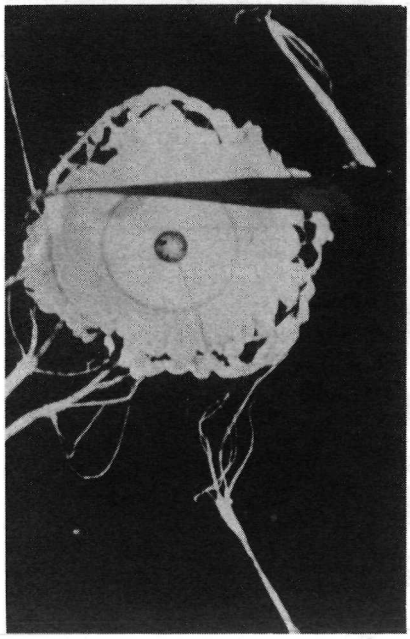

Frame 123, t' = 1.959 sec

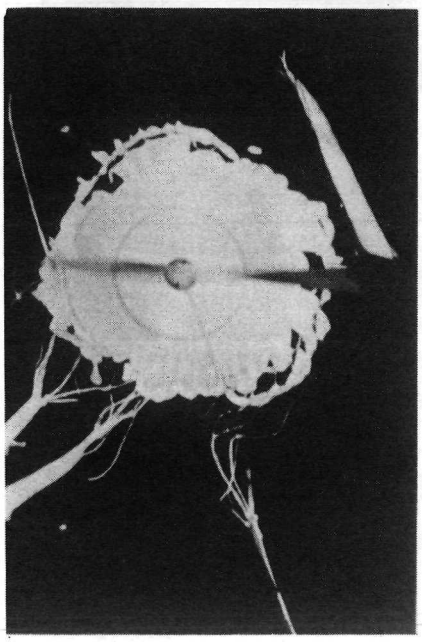

Frame 124, t' = 1.975 sec

L-72-6599

(d) Continued.

Figure 18.- Continued.

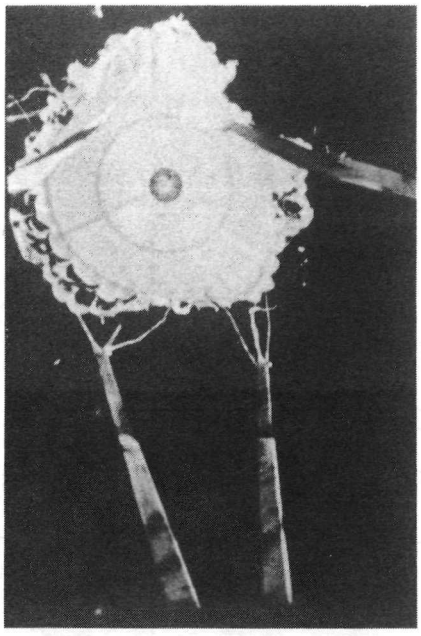

Frame 192, t' = 3.057 sec

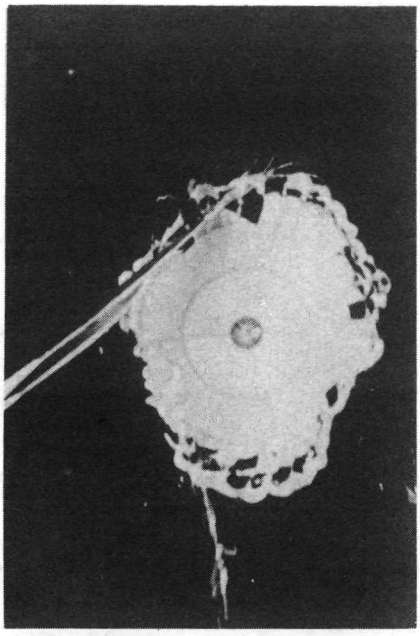

Frame 218, t' = 3.471 sec

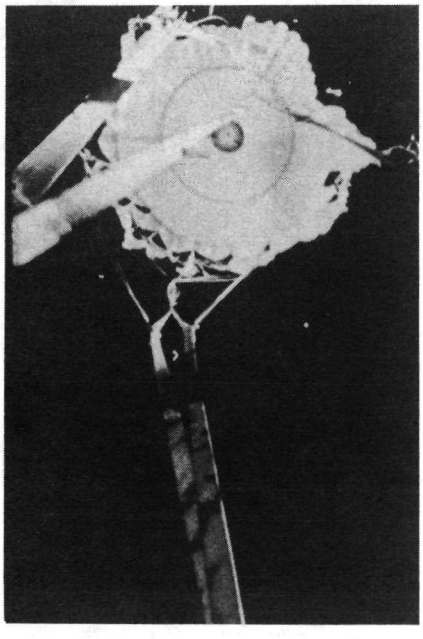

Frame 224, t' = 3.567 sec

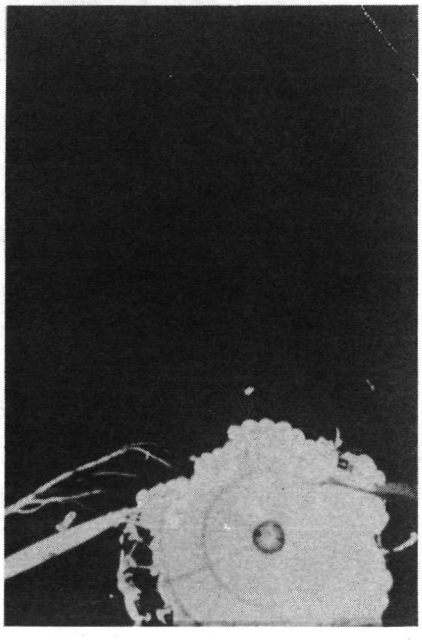

Frame 241, t' = 3.838 sec

L-72-6600

(d) Concluded.

Figure 18.- Concluded.

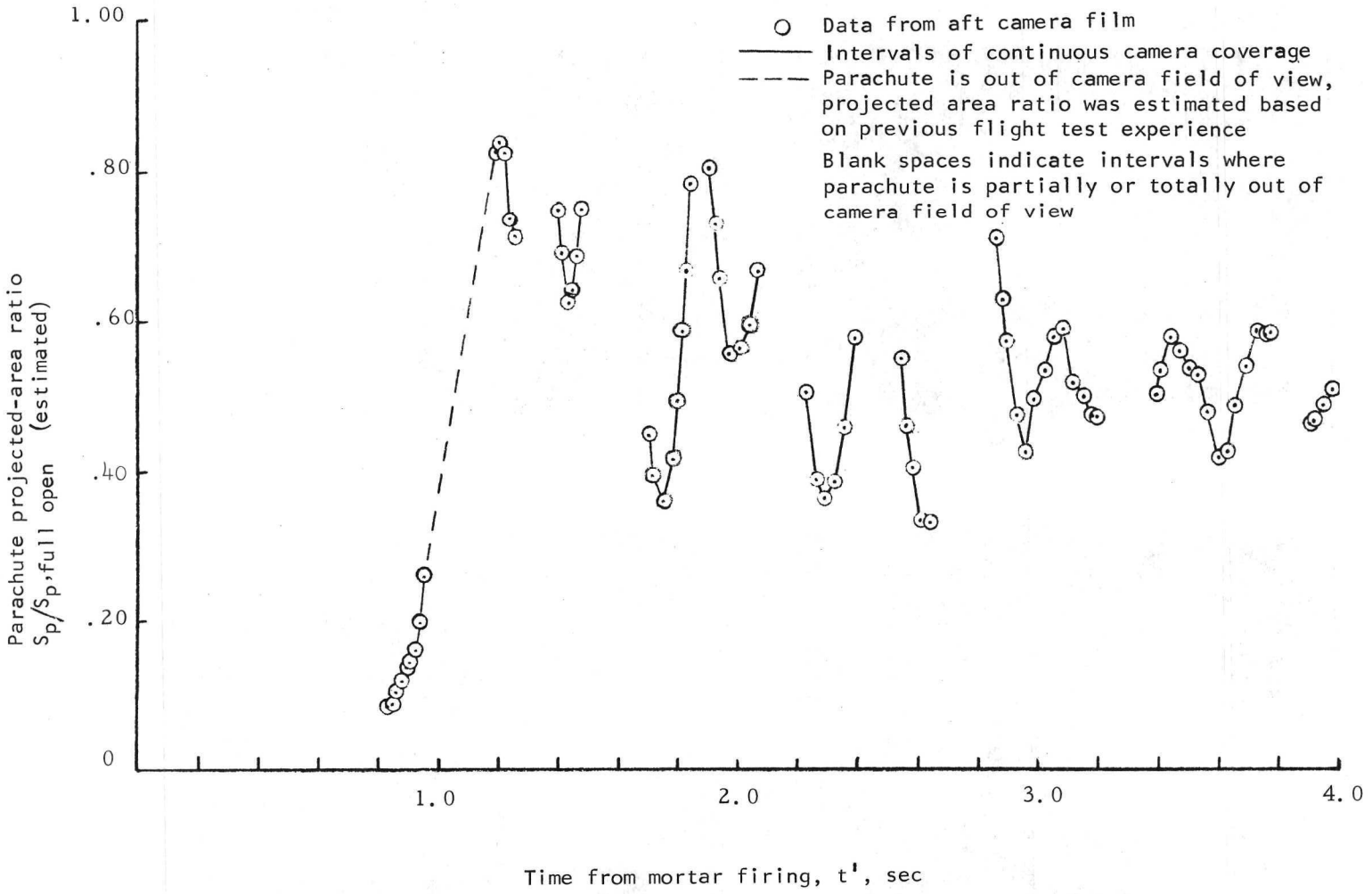

Figure 19.- Parachute projected-area ratio during deployment and initial test period.

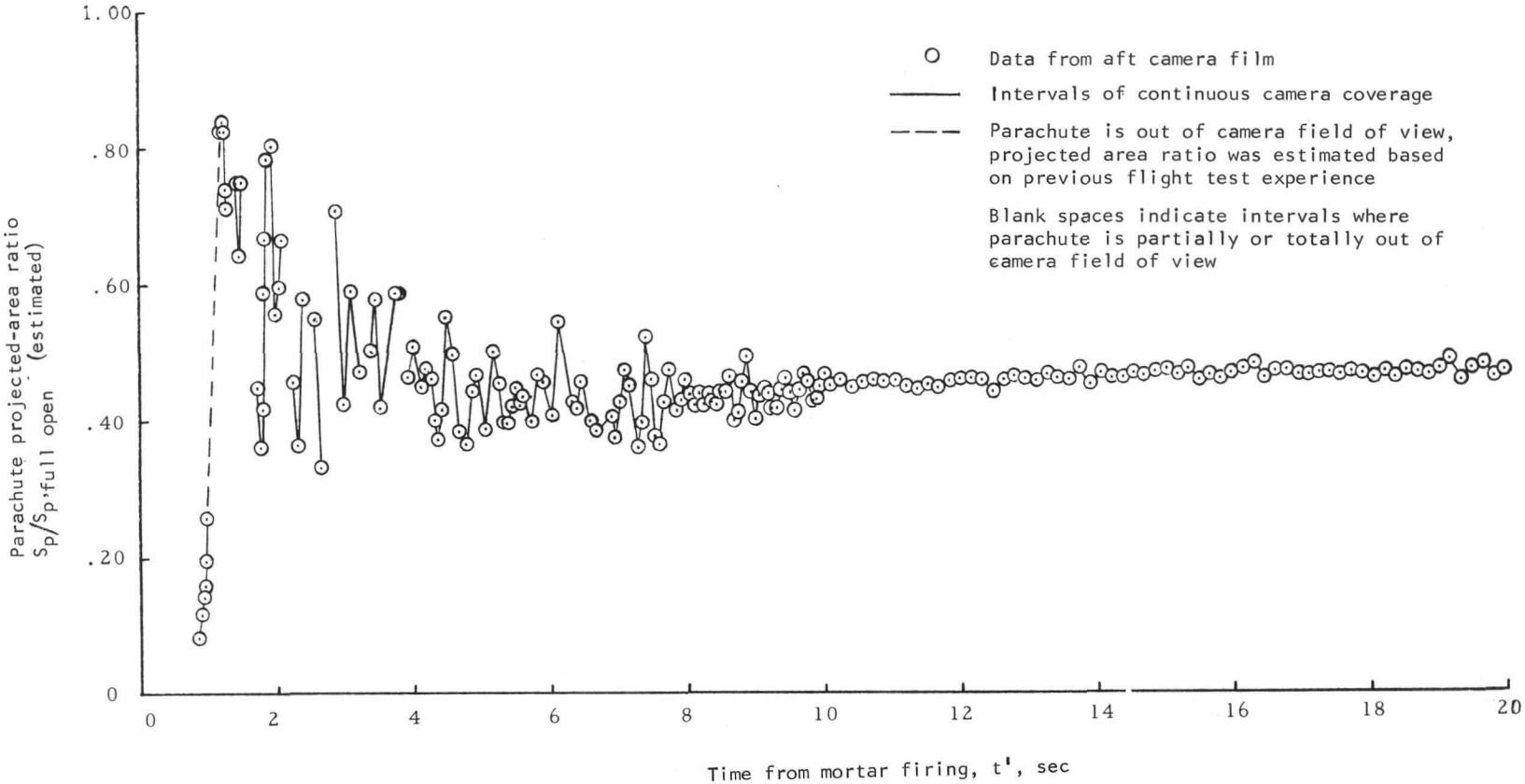

Figure 20.- Parachute projected-area ratio for first 20 seconds of operation.

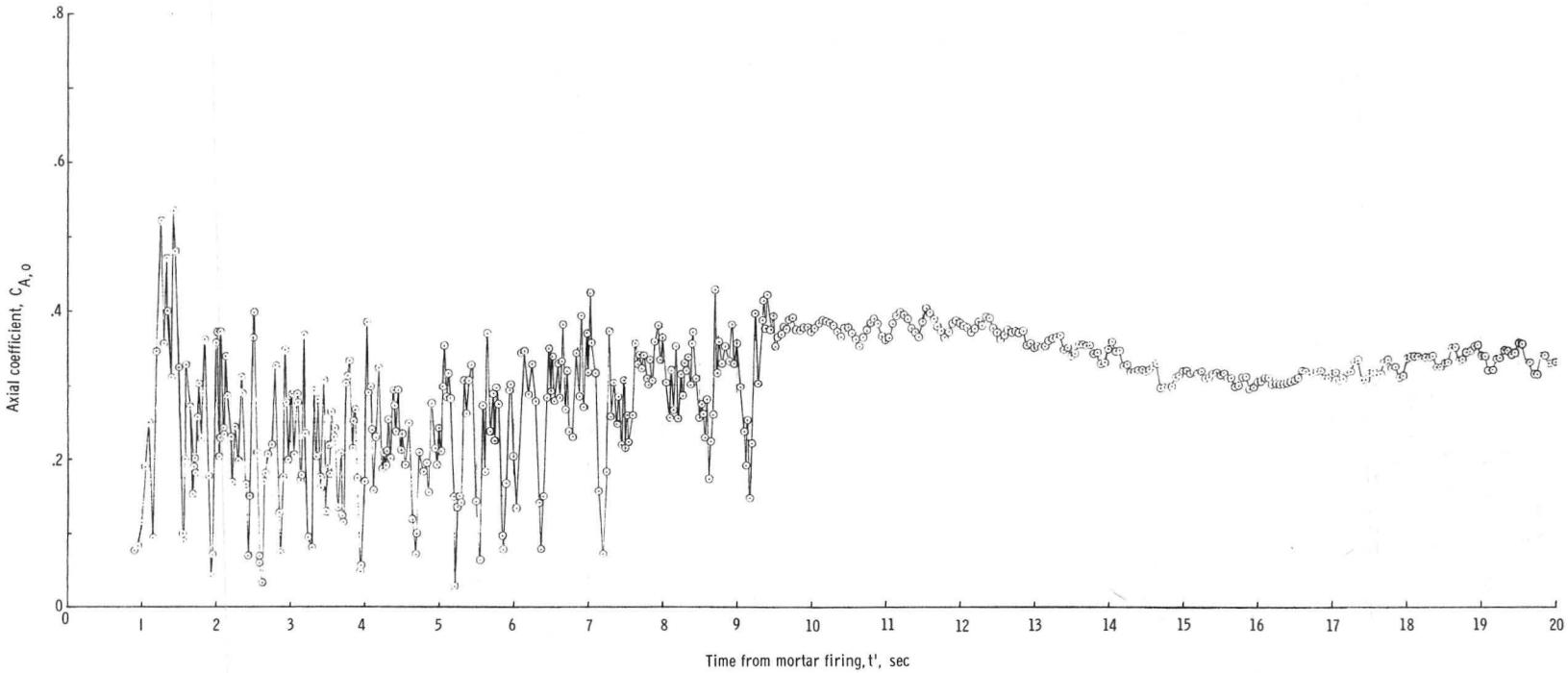

Figure 21.- Parachute axial-force coefficient as a function of time.

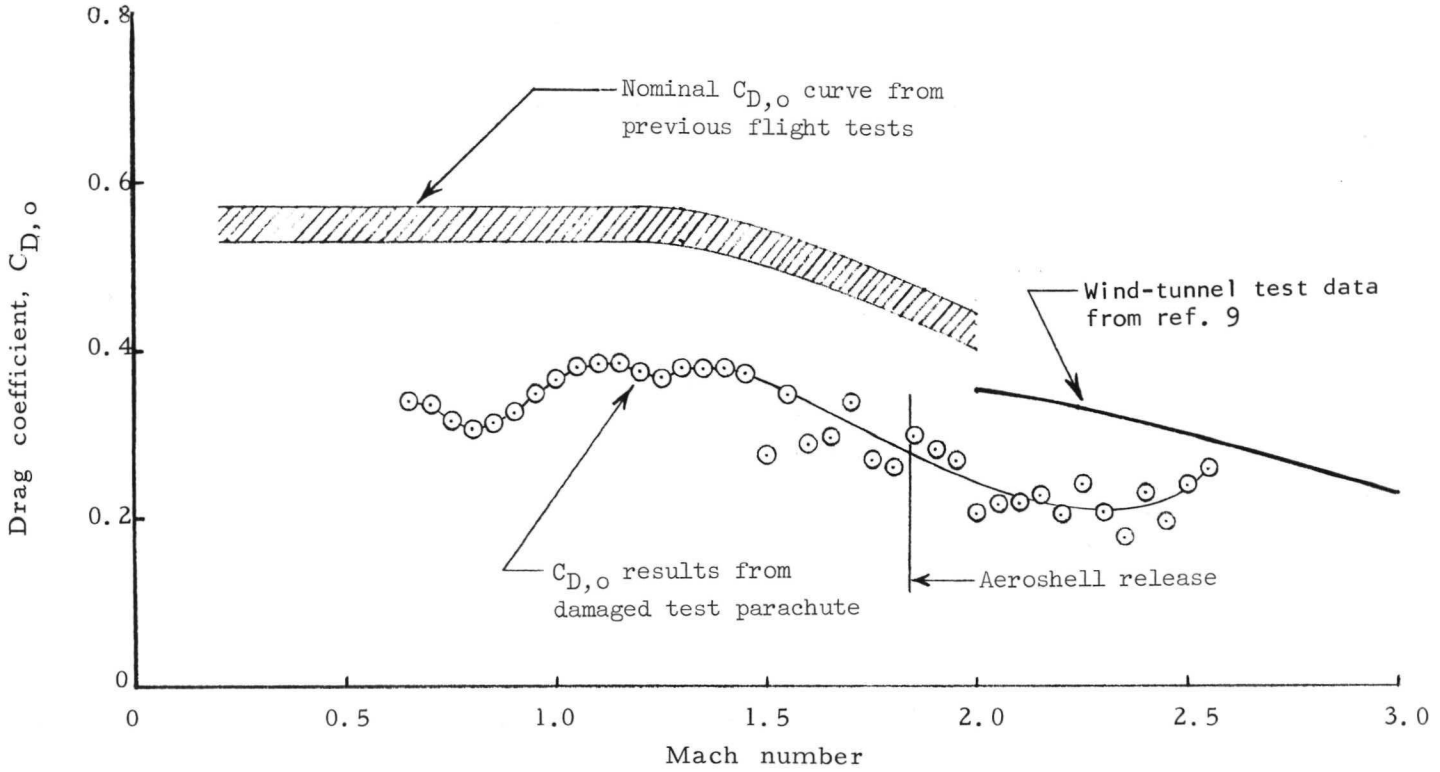

Figure 22.- Drag coefficient $C_{D,o}$ as a function of Mach number.

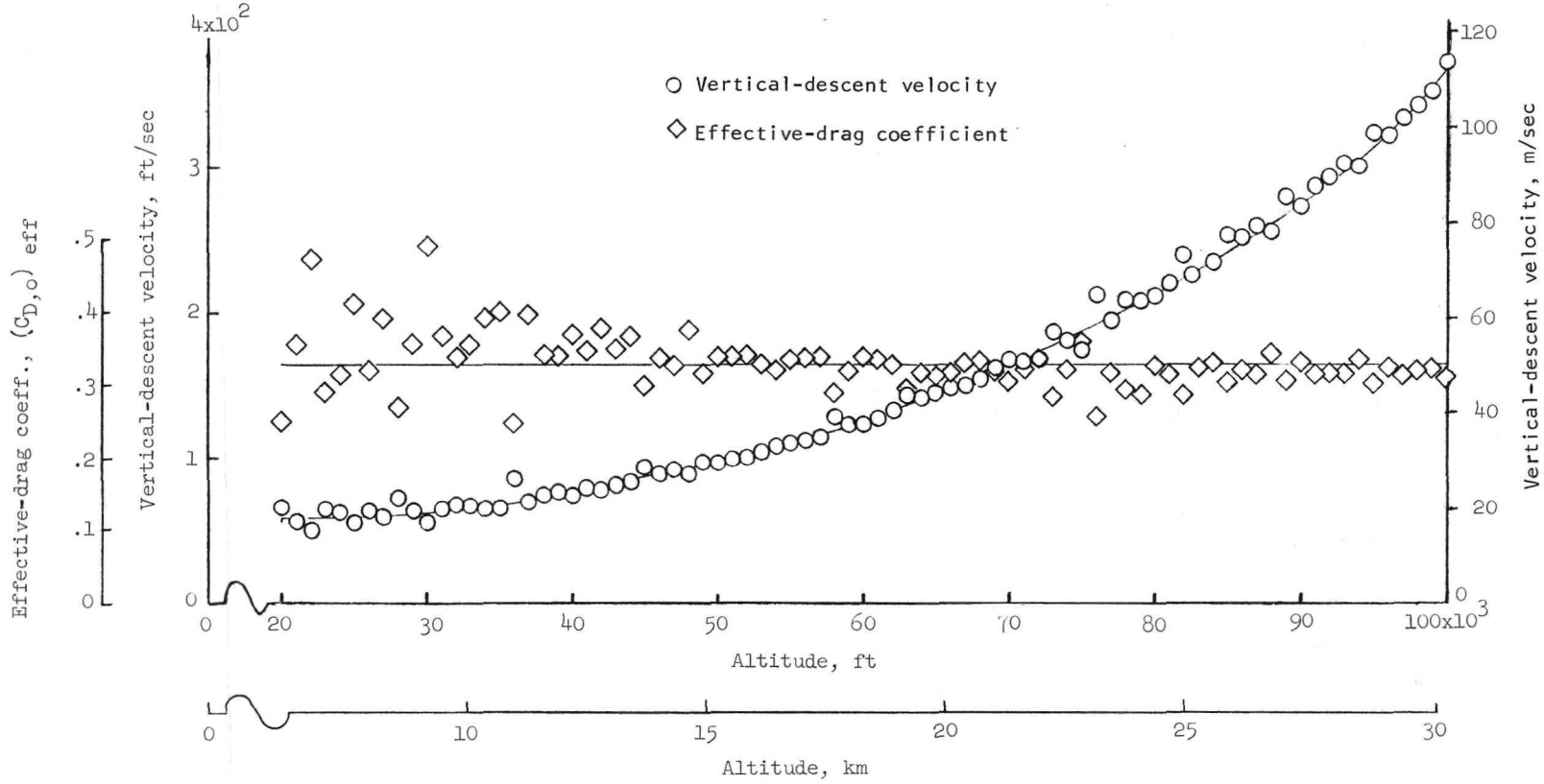

Figure 23.- Variation of vertical-descent velocity and effective-drag coefficient with altitude.

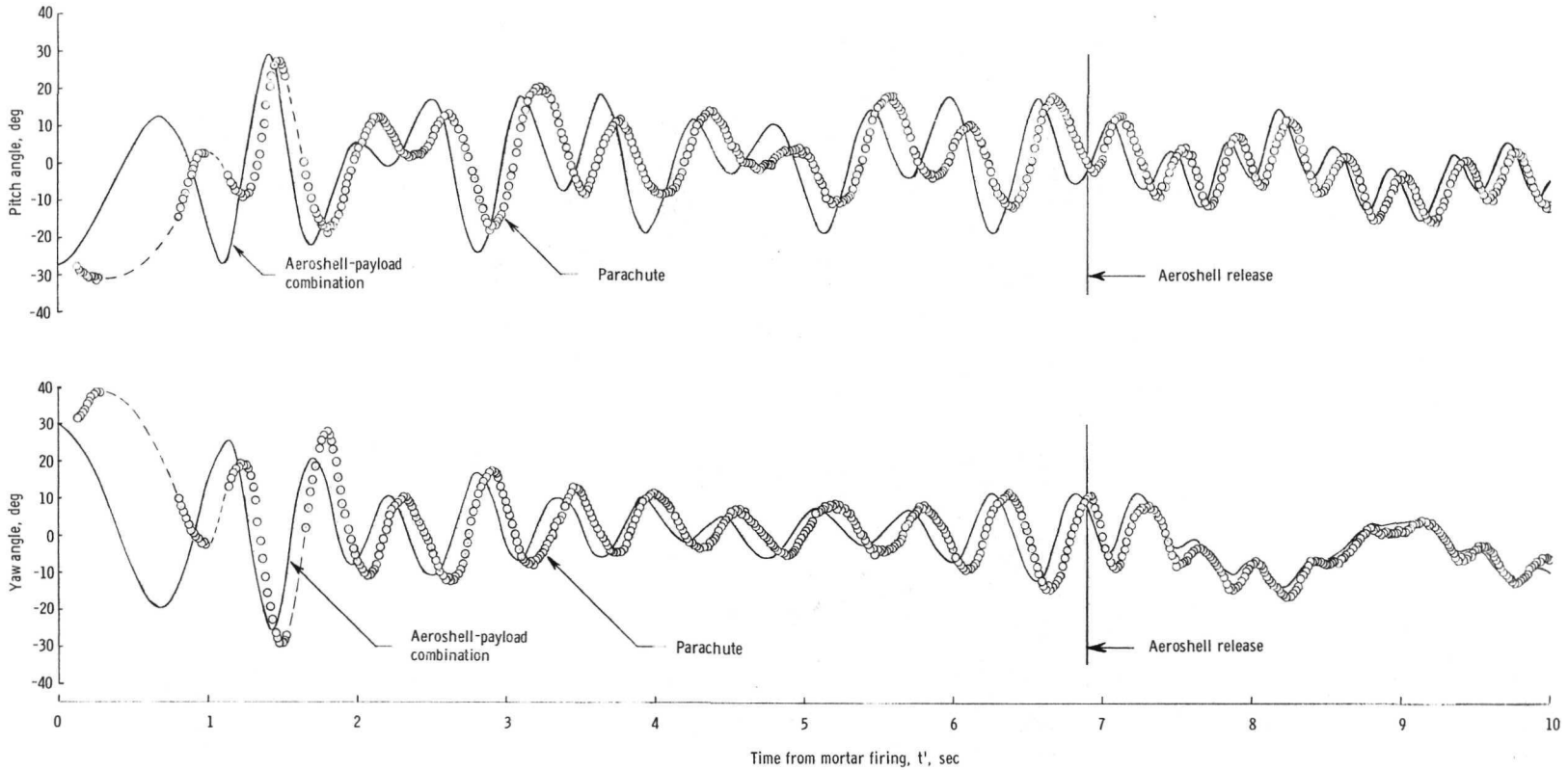

Figure 24.- Payload and parachute pitch and yaw angle with respect to vehicle flight path.

L-71-2676

Figure 25.- Photograph showing typical damaged areas of parachute canopy.

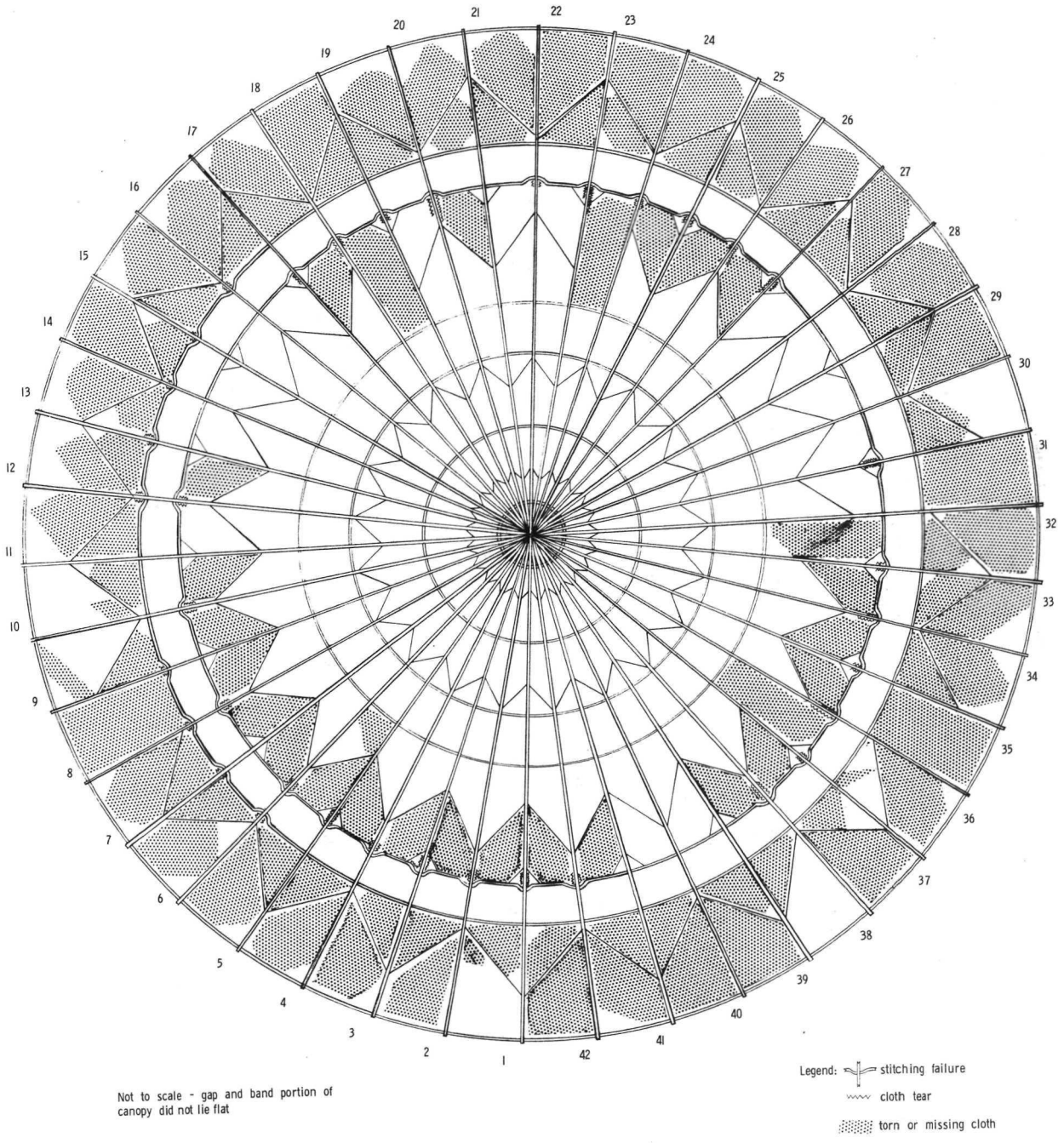

Figure 26.- Sketch showing canopy damage.

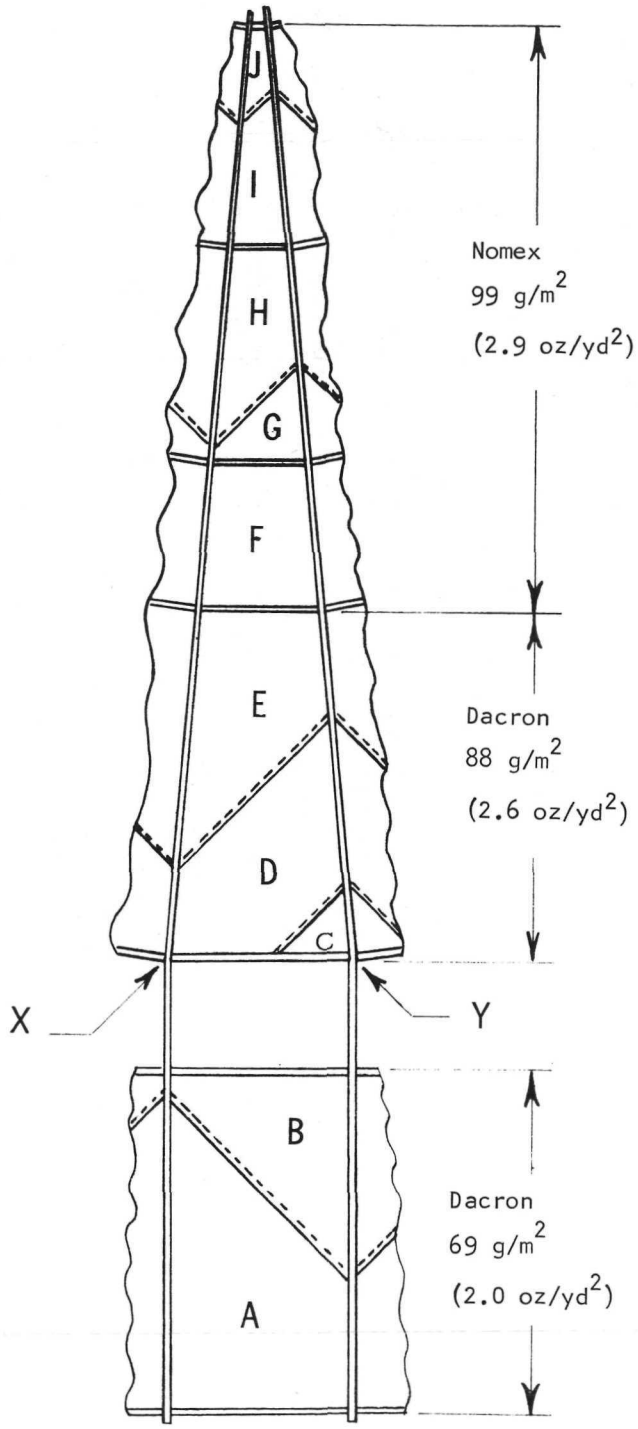

Figure 27.- Parachute gore-part identification.

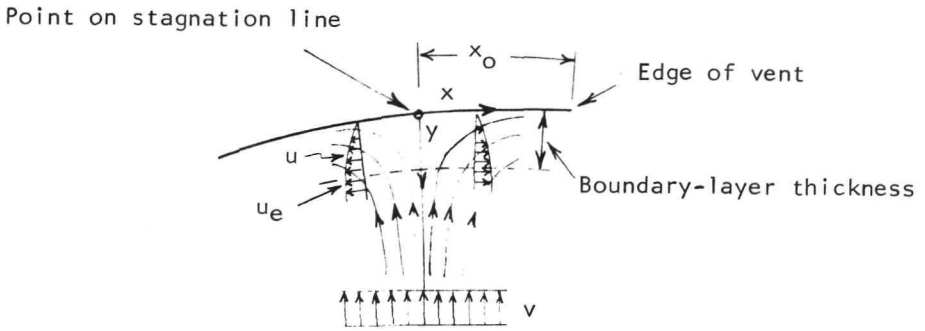

(a) Sketch illustrating notation and flow in vicinity of stagnation line.

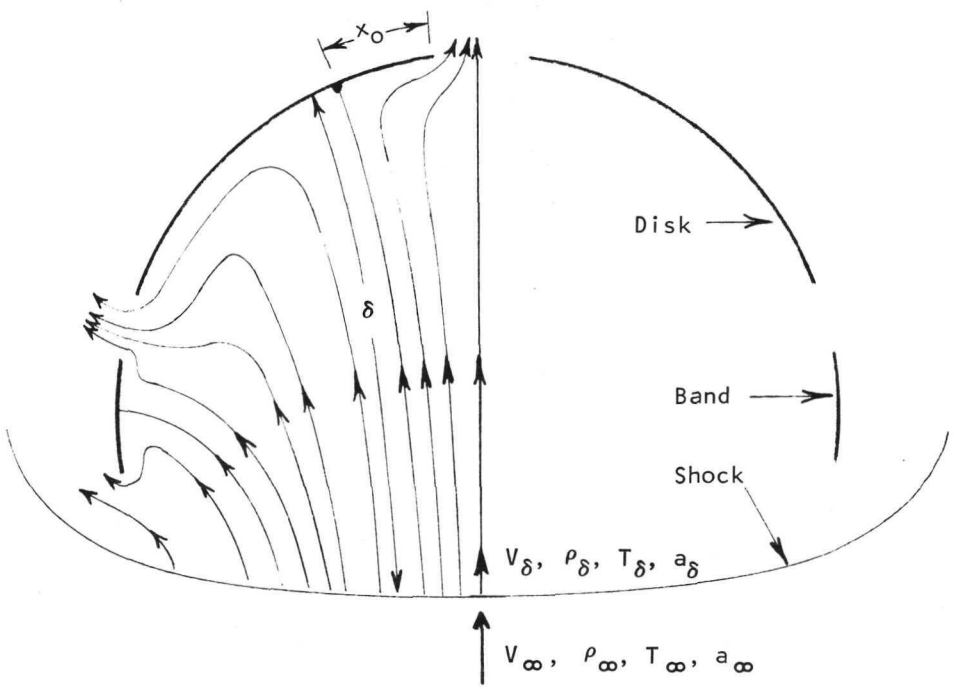

(b) Cross section of fully inflated disk-gap-band parachute canopy with assumed streamline pattern.

Figure 28.- Sketches illustrating flow in vicinity of stagnation line and interval to fully inflated disk-gap-band parachute.

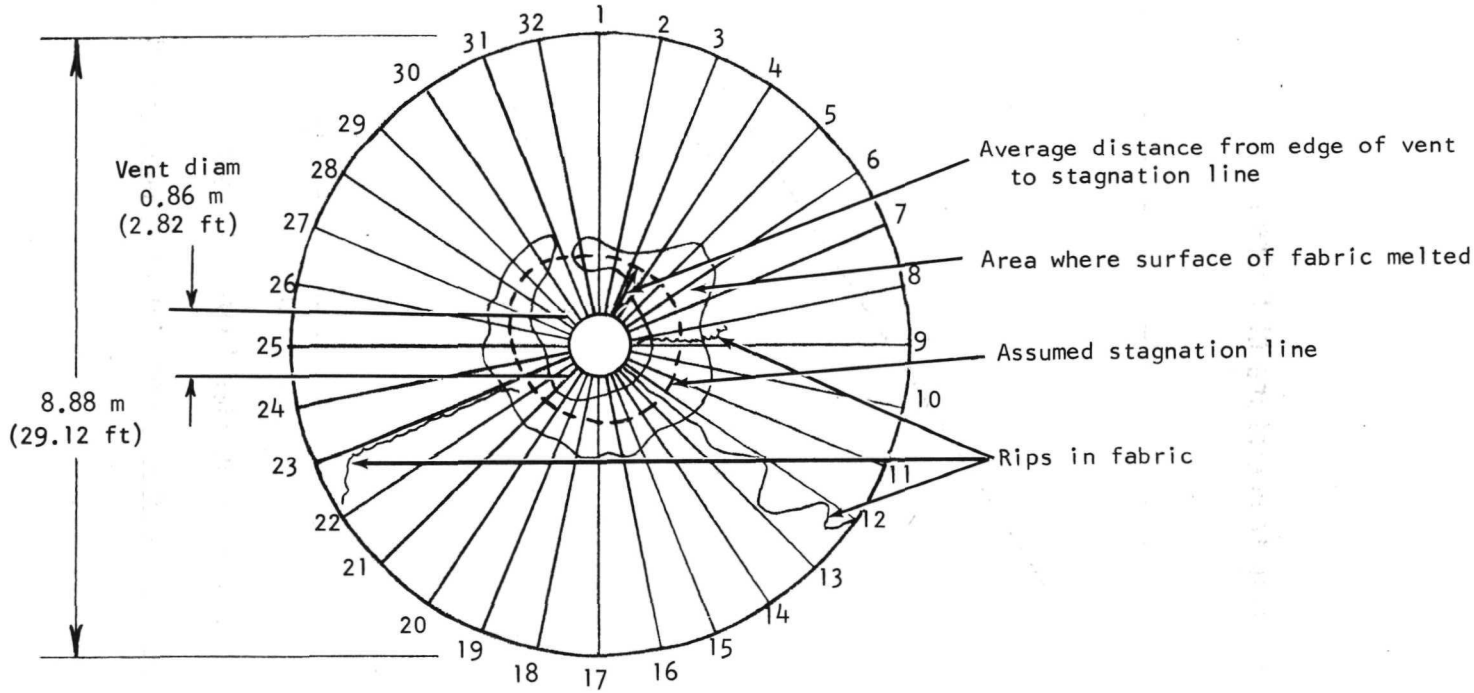

Figure 29.- Features of disk of 12.2-m-nominal-diameter (40-ft) disk-gap-band parachute subsequent to Mach number 3.31 deployment flight.

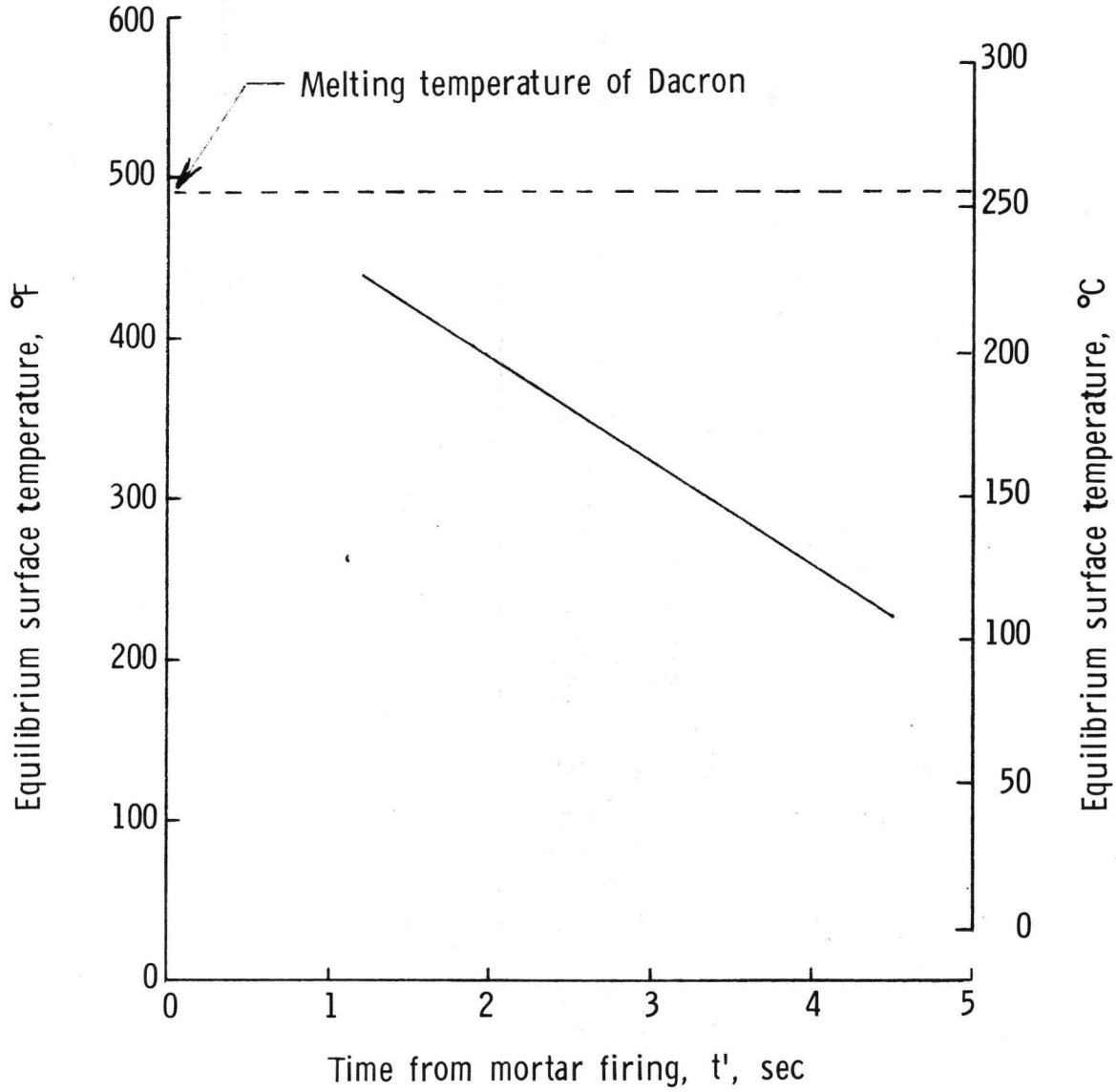

Figure 30.- Equilibrium surface temperature for anticipated worst case trajectory.

NATIONAL AERONAUTICS AND SPACE ADMINISTRATION
WASHINGTON, D.C. 20546

OFFICIAL BUSINESS
PENALTY FOR PRIVATE USE $300

SPECIAL FOURTH-CLASS RATE
BOOK

POSTAGE AND FEES PAID
NATIONAL AERONAUTICS AND
SPACE ADMINISTRATION
451

U.S.MAIL

POSTMASTER: If Undeliverable (Section 158 Postal Manual) Do Not Return

"The aeronautical and space activities of the United States shall be conducted so as to contribute . . . to the expansion of human knowledge of phenomena in the atmosphere and space. The Administration shall provide for the widest practicable and appropriate dissemination of information concerning its activities and the results thereof."

—NATIONAL AERONAUTICS AND SPACE ACT OF 1958

NASA SCIENTIFIC AND TECHNICAL PUBLICATIONS

TECHNICAL REPORTS: Scientific and technical information considered important, complete, and a lasting contribution to existing knowledge.

TECHNICAL NOTES: Information less broad in scope but nevertheless of importance as a contribution to existing knowledge.

TECHNICAL MEMORANDUMS: Information receiving limited distribution because of preliminary data, security classification, or other reasons. Also includes conference proceedings with either limited or unlimited distribution.

CONTRACTOR REPORTS: Scientific and technical information generated under a NASA contract or grant and considered an important contribution to existing knowledge.

TECHNICAL TRANSLATIONS: Information published in a foreign language considered to merit NASA distribution in English.

SPECIAL PUBLICATIONS: Information derived from or of value to NASA activities. Publications include final reports of major projects, monographs, data compilations, handbooks, sourcebooks, and special bibliographies.

TECHNOLOGY UTILIZATION PUBLICATIONS: Information on technology used by NASA that may be of particular interest in commercial and other non-aerospace applications. Publications include Tech Briefs, Technology Utilization Reports and Technology Surveys.

Details on the availability of these publications may be obtained from:

SCIENTIFIC AND TECHNICAL INFORMATION OFFICE

NATIONAL AERONAUTICS AND SPACE ADMINISTRATION

Washington, D.C. 20546